Cell Reports

Article

Behavioral state and stimulus strength regulate the role of somatostatin interneurons in stabilizing network activity

Graphical abstract

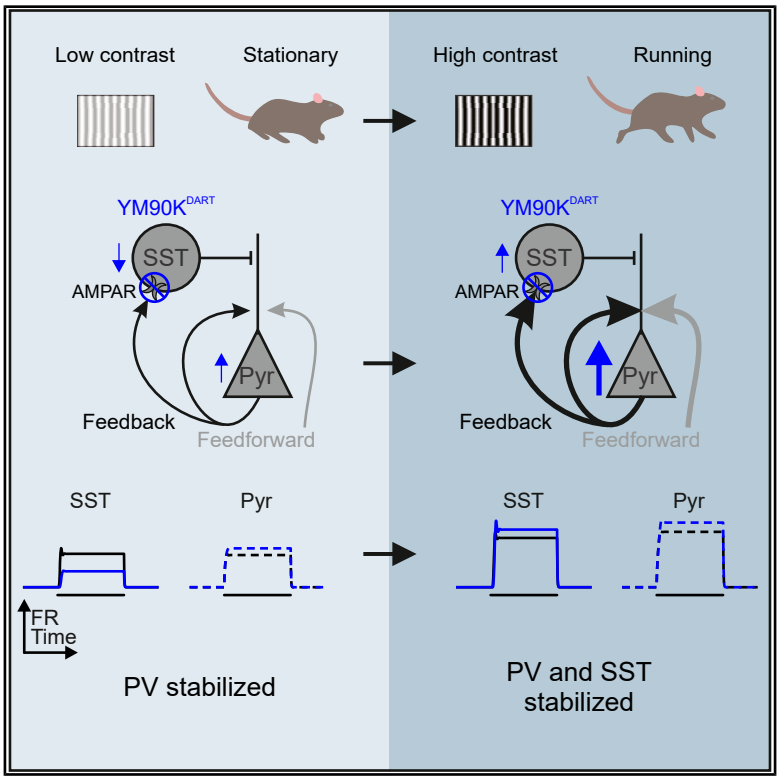

Authors

Celine M. Cammarata, Yingming Pei, Tingwei Hu, ..., Nicolas Brunel, Michael R. Tadross, Lindsey L. Glickfeld

Correspondence

glickfeld@neuro.duke.edu

In brief

Inhibition enables cortical stability, yet which classes of interneurons contribute to stabilization across conditions is not known. Cammarata et al. reveal that somatostatin interneurons in mouse V1 are selectively required for network stability during high input and arousal. Thus, the cortex inhabits multiple different stabilization regimes.

Highlights

- Blocking AMPARs on SST cells decreases their responses to weak stimuli during quiescence
- The same manipulation facilitates SST responses to strong stimuli during locomotion
- A V1 model recapitulates the context dependence of SST cells' role in network stabilization
- Cortical operating regime is defined by both sensory input and behavioral state

Cammarata et al., 2025, Cell Reports *44*, 115954
July 22, 2025 © 2025 The Author(s). Published by Elsevier Inc.
https://doi.org/10.1016/j.celrep.2025.115954

CellPress

Cell Reports

CellPress
OPEN ACCESS

Article

Behavioral state and stimulus strength regulate the role of somatostatin interneurons in stabilizing network activity

Celine M. Cammarata,[1] Yingming Pei,[1] Tingwei Hu,[1] Brenda C. Shields,[2] Shaun S.X. Lim,[2] Tammy Hawley,[1] Jennifer Y. Li,[1] David St. Amand,[1] Nicolas Brunel,[1,3,4,5] Michael R. Tadross,[2,5] and Lindsey L. Glickfeld[1,6,*]

[1]Department of Neurobiology, Duke University Medical Center, Durham, NC 27710, USA
[2]Department of Biomedical Engineering, Duke University, Durham, NC 27701, USA
[3]Department of Physics, Duke University, Durham, NC 27710, USA
[4]Department of Computing Sciences, Bocconi University, Milan 20136, Italy
[5]These authors contributed equally
[6]Lead contact
*Correspondence: glickfeld@neuro.duke.edu
https://doi.org/10.1016/j.celrep.2025.115954

SUMMARY

Inhibition stabilization enables cortical circuits to encode sensory signals across diverse contexts. Somatostatin-expressing (SST) interneurons are well suited for this role through their strong recurrent connectivity with excitatory pyramidal cells. We tested the necessity of SST cells for inhibition stabilization in mouse primary visual cortex by selectively blocking excitatory glutamatergic receptors on SST cells. Antagonizing this key input for the recruitment of SST cells drives a paradoxical facilitation of their activity—the hallmark of inhibition stabilization—with increasing stimulus contrast, and even more so with high arousal. In a computational model of the visual cortex circuit, increasing sensory input and arousal both move the network toward a regime where other classes of interneurons are no longer sufficient for maintaining network stability. Thus, we reveal that the role of SST cells in cortical processing gradually switches as a function of both input strength and behavioral state.

INTRODUCTION

Normalization is a key function of sensory cortices that allows detection of weak stimuli while preventing saturation to strong stimuli.[1–3] One proposed mechanism for normalization is through amplification of weak inputs via recurrent excitation, which is stabilized by recurrent inhibition as inputs strengthen. Such a network that requires inhibition to avoid runaway excitation is known as an "inhibition-stabilized network" (ISN). A hallmark of an ISN is the paradoxical effect following perturbation of inhibitory interneurons, wherein excitation results in their suppression while suppression yields excitation.[4–7] A growing body of work across mice, cats, and primates indicates that auditory, somatosensory, motor, and visual cortices exhibit paradoxical responses to optogenetic and visual perturbations, suggesting that the cortex generally operates as an ISN.[7–15] However, it remains poorly understood how the diverse cell types that comprise cortical circuits support inhibition stabilization.

Past research has emphasized the role of parvalbumin-expressing (PV) interneurons in stabilizing network activity.[5,10,13,14,16] These cells receive both feedforward and recurrent excitatory input and robustly inhibit the local excitatory pyramidal cells.[17–19] Empirically, optogenetic stimulation of PV cells yields the hallmark paradoxical suppression.[10,13,14] Moreover, computational modeling has suggested that the PV population is either the exclusive[5] or the predominant[16] inhibitory cell type responsible for inhibition stabilization.

Some models, however, indicate that PV cells may be insufficient to stabilize network activity when network excitation is high.[20,21] In such scenarios, network stabilization may additionally require inhibition from somatostatin-expressing (SST) interneurons, which are primarily driven by recurrent excitation from local pyramidal cells and in turn inhibit the pyramidal population.[18,22,23] SST cells are particularly well positioned to support PV cells in the ISN when network excitation is high as SST cells respond robustly to large, high-contrast stimuli[11,22,24,25] and have been implicated in shaping pyramidal output in high arousal states.[25–27] Indeed, optogenetic suppression of SST cells enhances inhibition onto neighboring pyramidal cells, consistent with perturbation of an ISN.[8,9]

We sought to test whether, and under what network conditions, SST cells are required for the ISN. We explored this in the mouse primary visual cortex (V1) using cell-type-specific pharmacology to partially block AMPA-type glutamate receptors (AMPARs) onto SST cells, thereby selectively reducing the input that connects SST cells to the local network. We find that this manipulation suppresses SST responses to weak visual stimuli, but the suppressive effect is attenuated by strong stimuli or

This is an open access article under the CC BY-NC-ND license (http://creativecommons.org/licenses/by-nc-nd/4.0/).

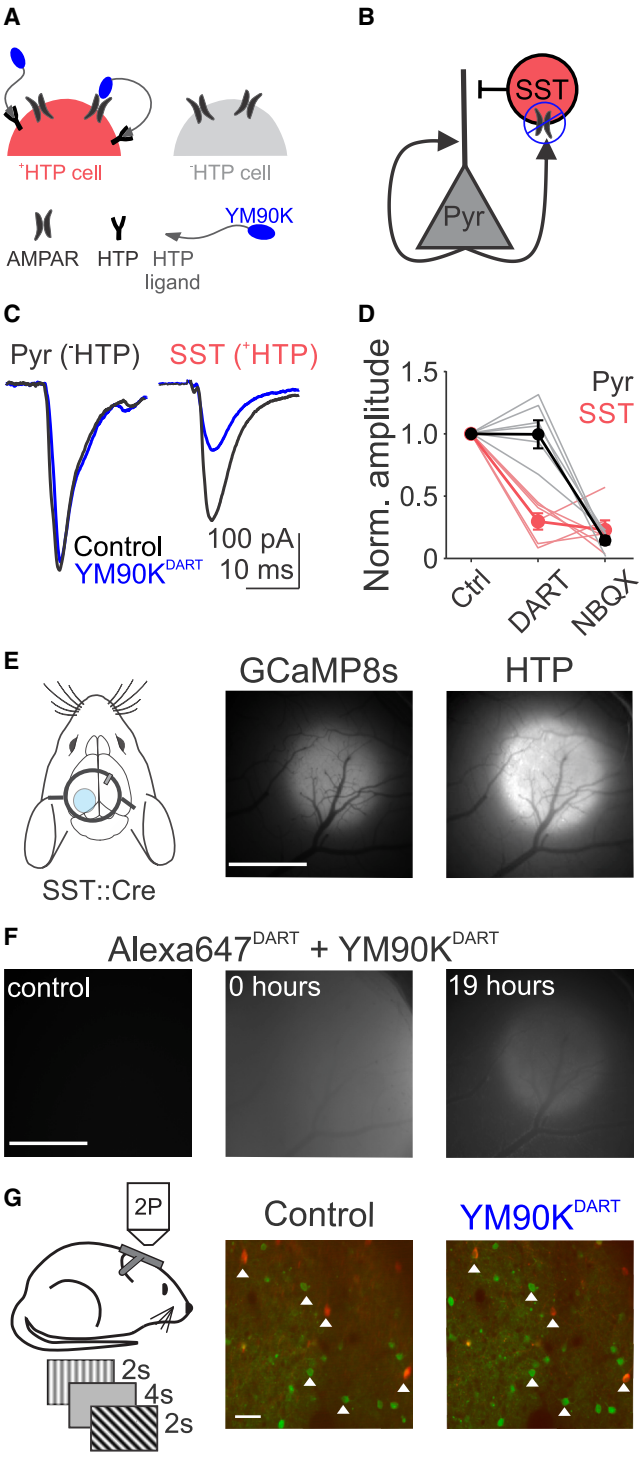

Figure 1. Cell-type-specific *in vivo* pharmacology of AMPARs with YM90K^{DART}

(A) Schematic of cell-type-specific pharmacology with YM90K^{DART}. HTP: Halo-tag protein.

(B) Schematic of circuit manipulation.

(C) Average EPSCs in an example simultaneously recorded pyramidal cell (left) and SST cell (right) before (black) and after (blue) infusion of 300 nM YM90K^{DART}.

(D) Summary of average (filled circles) and individual (light lines) EPSC amplitudes normalized to control (Ctrl) for pyramidal (black) and SST (red) cells in YM90K^{DART} and 10 μM NBQX (n = 6 pairs). Error is SEM across cells.

(E) Schematic of cranial window and infusion cannula (left), and wide-field imaging of the calcium indicator GCaMP8s (middle) and flex-dTomato-HTP (right). Scale bar, 1 mm.

(F) Alexa 647^{DART} (1:10 with YM90K^{DART}) capture before (left), immediately after (middle), and 19 h after (right) infusion for mouse in (E).

(G) Left, schematic of experimental setup. Example two-photon imaging field of view of GCaMP (green) and HTP (red) expression in control (middle) and after YM90K^{DART} infusion (right) for mouse in (E). White triangles highlight example cells identifiable across sessions. Scale bar, 200 μm.

See also Figure S1.

locomotion. Under these conditions, a subset of SST cells is paradoxically driven more strongly following reduction in glutamatergic input. This is likely due to the initial disinhibition driving stronger recurrent excitation to increase the drive to SST cells via the unblocked subset of glutamate receptors. To understand what changes in network activity underlie these observed paradoxical responses in SST cells, we developed a model of V1 including pyramidal, SST, PV, and vasointestinal peptide-expressing (VIP) cells. Our model indicates that while PV cells are sufficient to stabilize the cortex when sensory inputs are weak, SST cells are required with increasing input. Our model further reveals that the paradoxical effects we observe empirically with increasing contrast and locomotion are due to the emergence of a network state where stability demands inhibition from SST cells. While the effects of contrast are well fit by solely increasing input to the network, the effects of locomotion additionally require changes to local network interactions. These results elucidate the conditions under which SST cells are necessary to stabilize visual cortex circuits.

RESULTS

Cell-type-specific antagonism of AMPARs

To selectively block excitatory input onto SST cells, antagonizing the connection that recruits interneurons for stabilization of local networks, we used the cell-type-specific pharmacological approach, Drug Acutely Restricted by Tethering[28,29] (DART; Figures 1A and 1B). We virally expressed the HaloTag protein (HTP) in V1 of SST::Cre mice to antagonize AMPARs on SST cells upon introduction of YM90K.1$^{DART.2}$ (YM90K^{DART}). *In vitro* whole-cell recordings reveal that acute application of YM90K^{DART} significantly reduces the amplitude of evoked excitatory postsynaptic currents (EPSCs) onto HTP-expressing ($^{+}$HTP) SST cells to approximately 40% of control (paired t test with Bonferroni correction, $p < 0001$; Figures 1C and 1D) without affecting simultaneously recorded $^{-}$HTP pyramidal cells ($p = 1$). Subsequent application of the non-selective AMPAR antagonist NBQX significantly reduced EPSC amplitude on pyramidal cells (paired t test with Bonferroni correction, $p = 0.021$) but not SST cells ($p = 1$), suggesting little remaining AMPA-mediated excitation (Figure 1D). Similarly, incubation of slices in YM90K^{DART} reduces the frequency (two-way ANOVA main effect of drug, $p < 0.001$; Figures S1A and S1B) of spontaneous EPSCs onto $^{+}$HTP SST cells compared to controls. The amplitude of the remaining spontaneous EPCS trends toward reduction although

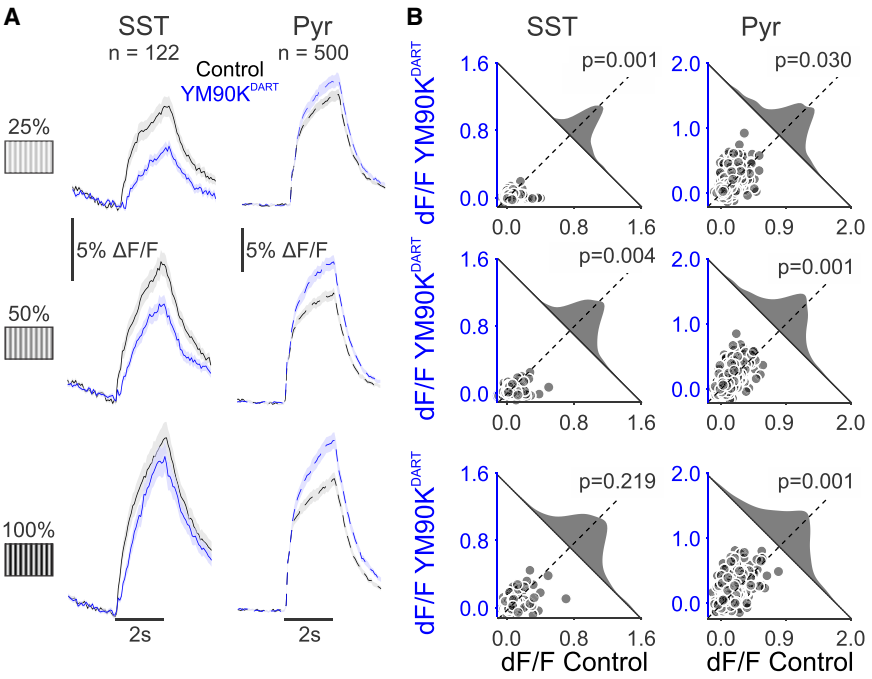

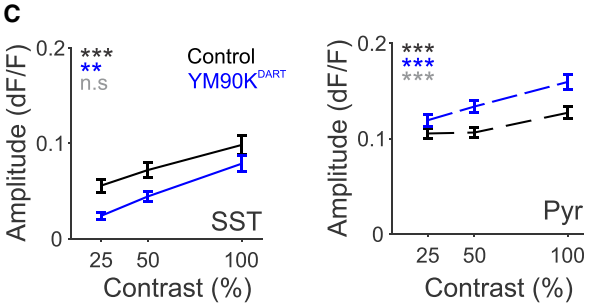

Figure 2. The effect of blocking AMPARs on SST cells depends on stimulus strength

(A) Grand average time courses for $^{+}$HTP SST (left, solid lines) and $^{-}$HTP putative pyramidal cells (right, dotted lines) before (black) and after (blue) YM90K^{DART} infusion, in response to preferred-direction gratings (horizontal black bar) at 25% (top), 50% (middle), and 100% (bottom) stimulus contrast, during stationary epochs. Shaded error is SEM across cells.

(B) Mean response during the stimulus period in control and after YM90K^{DART} for all SST (left) and pyramidal (right) cells. Histogram is the probability distribution of ratios of responses in control and after YM90K^{DART}. Dashed line is unity line. *p* values are from paired t test.

(C) Mean response during stimulus period, for SST cells (left) and pyramidal cells (right) before (black) and after (blue) YM90K^{DART} infusion, at each contrast. Error is SEM across cells. *p* values are from two-way ANOVA: main effect of contrast (black), drug (blue), and interaction (gray). n.s., not significant; $^{**}p < 0.01$; $^{***}p < 0.001$.

See also Figure S2.

it does not reach significance (unpaired t test, $p = 0.073$; Figure S1C). This reduction of EPSC amplitude is robust when YM90K^{DART} is infused *in vivo* via the cisterna magna (unpaired t test, $p = 0.003$; Figures S1D–S1F) or when trains of EPSCs are evoked at high frequency driving short-term synaptic facilitation (50 Hz; one-way ANOVA, effect of stimulus number, $p = 0.99$; Figures S1G–S1I). These data support a specific and robust effect of YM90K^{DART} on $^{+}$HTP SST cells.

To probe the effects of blocking excitatory input to SST cells *in vivo*, we pan-neuronally expressed GCaMP8s alongside cell-type-specific expression of HTP on SST cells in V1 and delivered DART ligands via a cannula in the contralateral ventricle (Figure 1E). Co-infusion of a mixture of YM90K^{DART} and Alexa 647^{DART} enables visualization of ligand delivery and subsequent capture using wide-field imaging through the cranial window[29] (Figure 1F). Post hoc histology reveals robust and selective ligand capture on $^{+}$HTP cells (Figures S1J–S1L).

The effect of blocking AMPARs on SST cells depends on stimulus strength

We used two-photon microscopy to record the activity of populations of $^{+}$HTP SST cells and neighboring putative pyramidal cells in layer 2/3 of V1 while mice passively viewed full-field sinusoidal gratings (2 Hz, 0.1 cycles per degree) moving in one of eight directions (45° increments) at one of three contrasts (25%, 50%, and 100%; Figure 1G). Data were collected from the same neurons on consecutive days to measure visual responses in control conditions and 17–24 h after infusion of YM90K^{DART}.

The magnitude of the effect of blocking AMPARs on SST cells depends on the strength of the visual stimulus. When mice are stationary and the stimulus contrast is low, the SST population has a decreased visual response following YM90K^{DART} ($n = 122$ cells, 10 mice; paired t test with Bonferroni correction, $p < 0.001$, Figures 2A and 2B, top left), consistent with the decrease of excitatory drive. However, with increasing contrast, the effect of YM90K^{DART} on SST cells is diminished, such that there is no significant effect at full contrast ($p = 0.219$; Figures 2A and 2B, bottom left). We do not think that this stimulus dependence results from elevated glutamate release outcompeting YM90K^{DART} because the effect on the pyramidal cell population increases with increasing contrast ($n = 500$ cells; two-way ANOVA, interaction of contrast and YM90K^{DART}, $p = 0.001$; Figure 2C). This argues that the network effects of YM90K^{DART} are actually greater at high contrast, despite the apparent decreased effect on the average response of SST cells. To account for the statistical non-independence of neurons recorded from the same mouse, we complemented our ANOVA with mixed-effects models. These analyses qualitatively recapitulated our initial results (Table S1A).

To understand why the average effects on SST cells decrease, we investigated the effects on individual cells. The activity of individual SST cells is more strongly modulated by YM90K^{DART}

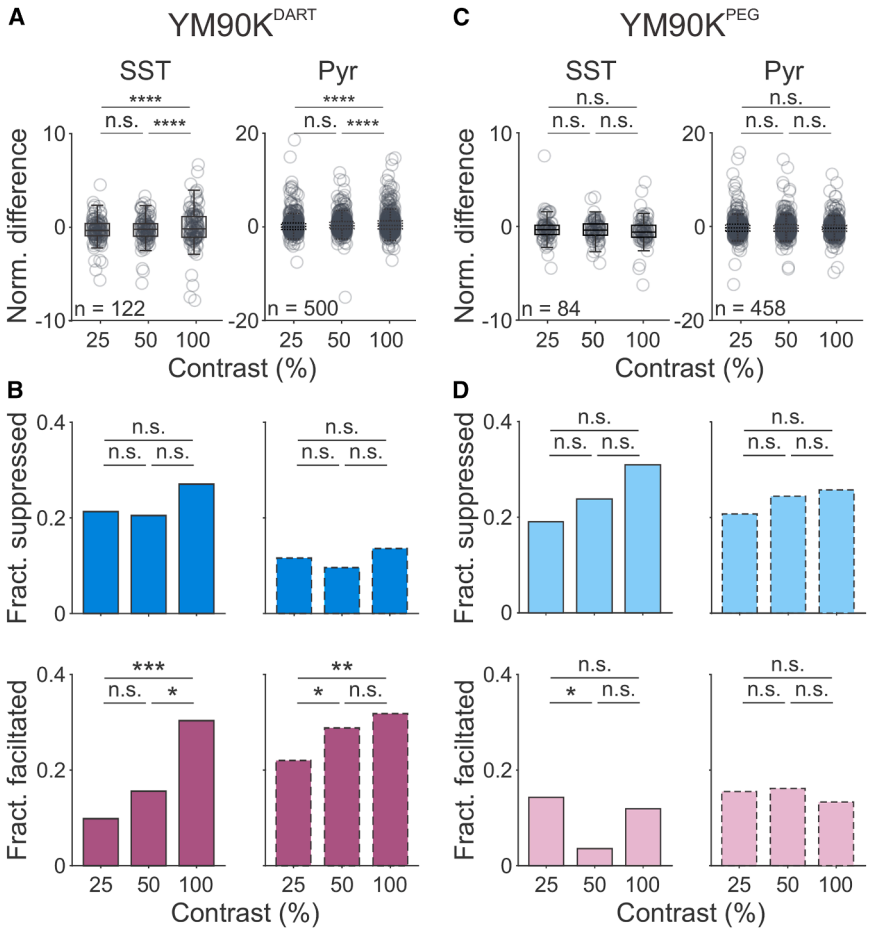

Figure 3. Decreased suppression of SST cells by YM90K^{DART} is consistent with an increase in the role of SST cells for stabilization

(A) Normalized difference ($\frac{mean_{DART} - mean_{control}}{STD_{control}}$) of stimulus response for SST (left) and pyramidal cells (right) as a function of contrast in YM90K^{DART}. Gray circles are individual cells; boxplots illustrate median, 25% and 75% quartiles. Significance refers to pairwise F tests for variance.

(B) Fraction of SST (left) and pyramidal (right) cells that are suppressed (top, cyan) or facilitated (bottom, magenta) by more than 1 std of their control response at each contrast.

(C and D) Same as (A) and (B), for YM90K^{PEG}.

n.s., not significant; *p < 0.05; **p < 0.01; ***p < 0.001; ****p < 0.0001. See also Figure S2.

with increasing contrast (Levene's test for unequal variance, p = 0.001; Figure 3A). Namely, the fraction of SST cells that are significantly facilitated by YM90K^{DART} (defined as the mean response increasing more than one standard deviation from control) becomes greater with increasing contrast (chi-squared test with Bonferroni correction for 25% vs. 50%, p = 0.535; 25% vs. 100%, p < 0.001; 50% vs. 100%, p = 0.018; Figure 3B). This mirrors the increased fraction of pyramidal cells facilitated with greater contrast (25% vs. 50%, p = 0.041; 25% vs. 100%, p = 0.001; 50% vs. 100%, p = 0.960), consistent with inhibition stabilization. Conversely, there is no significant change in the fraction of SST cells that are significantly suppressed (decreased by more than one standard deviation from control: chi-square with Bonferroni correction p > 0.05 for all contrast comparisons), and only a small fraction of pyramidal cells are suppressed at any contrast. Thus, we observe diverse effects on individual SST cells, with some being suppressed but more being facilitated as contrast increases.

As a control for ambient-drug effects of YM90K^{DART} and habituation due to repeated imaging,[30,31] we performed the same experiment with YM90K^{PEG}, which is chemically identical except for its lack of an HTP ligand. This construct, which cannot bind to HTP, washes out by the time of imaging (n = 6 mice; Figures S1J–S1K). Unlike the effects of YM90K^{DART}, treatment with YM90K^{PEG} results in weak suppression of both SST (n = 84 cells; two-way ANOVA, main effect of YM90K^{PEG}, p = 0.001; Figure S2) and pyramidal (n = 458 cells; p = 0.003) responses, without contrast-dependent modulation of either cell type (all comparisons, $p \geq$ 0.05; Figures 3C and 3D; Table S2A). Thus, the observed contrast-dependent effects of YM90K^{DART} are due to its action on SST cells.

Together, these findings suggest that reducing excitatory input onto SST cells largely decreases SST responses at low contrast but paradoxically increases responses in a subset of SST cells at higher contrast. Stronger visual input results in more robust disinhibition of pyramidal cells, driving the SST cells more strongly via their remaining unblocked glutamate receptors and, ultimately, resulting in a net facilitation of their activity. This is consistent with SST cells being recruited to stabilize network activity as stimulus strength increases.

SST cells correlated with the local network are less suppressed by YM90K^{DART}

In an ISN, recurrent input from pyramidal cells recruits interneurons to stabilize the network.[6,32–34] Given the importance of this recurrent connection for engagement in an ISN, those SST cells that are most robustly recurrently connected should be the most susceptible to paradoxical effects.

Noise correlations can be used as a proxy for shared connectivity.[35,36] To estimate the strength of recurrent input onto each SST cell, we calculated the noise correlation between individual SST cells and the mean of all simultaneously recorded pyramidal cells during the control imaging session (Figure 4A). Correlation measures were pooled across stimulus conditions as we find no significant dependence on contrast (one-way ANOVA, p = 0.055).[37] This yields a range of correlation values across the SST population that we defined as weakly (R < 0.5; n = 67 cells; Figure S3A) or strongly correlated (R > 0.5; n = 55 cells), with

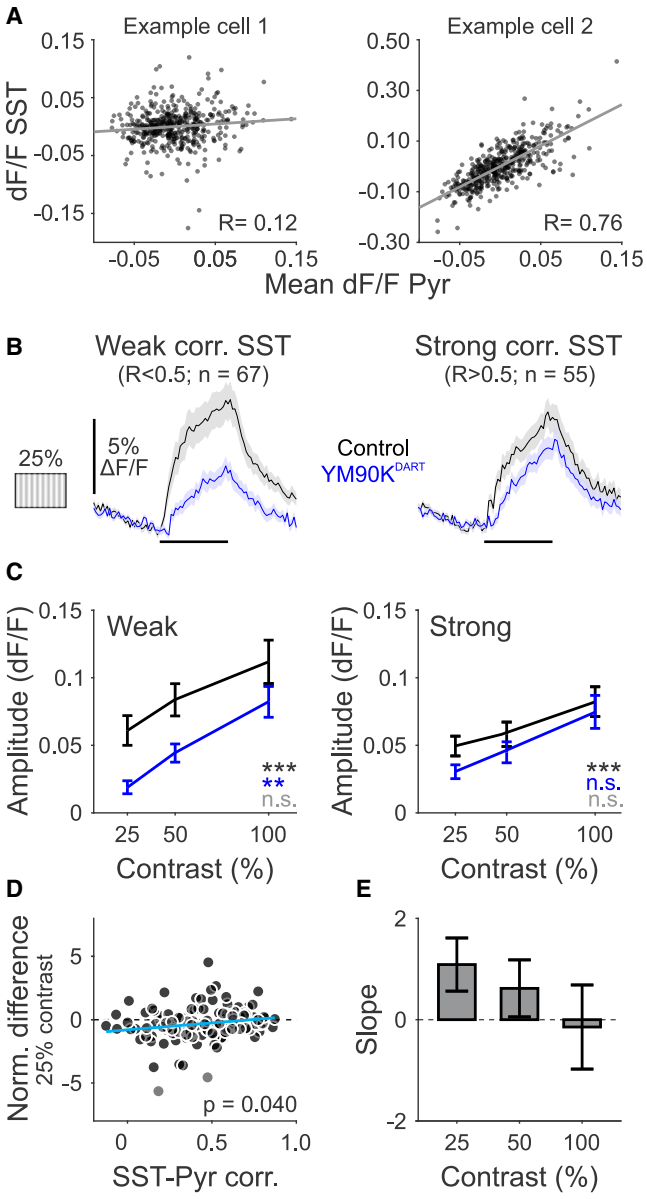

Figure 4. SST cells weakly correlated with the local network are more strongly suppressed by YM90K^{DART}

(A) Mean-subtracted trial-by-trial responses for two SST cells and concurrently recorded pyramidal cells. Each data point represents a single trial. Fit line is from a linear regression; R is the Pearson's correlation.

(B) Grand average time courses for SST cells before (black) and after (blue) YM90K^{DART} separated into those weakly (left) and strongly (right) correlated to pyramidal activity, during stationary epochs in response to preferred-direction gratings at 25% contrast. Shaded error is SEM across cells.

(C) Mean response during stimulus period, for SST cells weakly (left) or strongly (right) correlated to pyramidal activity, at each contrast in control (black) and after YM90K^{DART} (blue). Error is SEM across cells. *p* values are from two-way ANOVA: main effect of contrast (black), drug (blue), and interaction (gray).

(D) Scatter of noise correlation between each SST cell and the neighboring pyramidal cell population and the normalized difference at 25% contrast. Blue line and *p* value are from linear regression.

(E) Slope of the correlation in (D) for each contrast. Error is confidence interval. n.s., not significant; $^{*}p < 0.05$; $^{**}p < 0.01$.

See also Figure S3.

approximately half the SST cells in each experiment falling into each category (fraction strongly correlated, mean across mice ± standard deviation (std) = 46.67% ± 21.37%). We posit that SST cells that are more strongly correlated with pyramidal cells are likely to be more strongly recurrently connected and therefore less suppressed by YM90K^{DART}.

Consistent with our prediction, the weakly correlated SST cells have a significant decrease in visually evoked responses following YM90K^{DART} delivery (two-way ANOVA, main effect of YM90K^{DART}, $p = 0.004$; Figures 4B and 4C; Table S1B), whereas the strongly correlated SST cells are not significantly affected ($p = 0.114$). This relationship is also apparent in a linear regression showing that more strongly correlated SST cells are less suppressed—and more apt to be facilitated—by YM90K^{DART} in response to low-contrast stimuli ($p = 0.04$; Figure 4D). Notably, this relationship diminishes with increasing contrast (linear regression, $p = 0.034$; Figures 4E and S3B), consistent with the increasing recruitment of SST cells with weaker recurrent input into the ISN. The dependence on correlated variability is specific to YM90K^{DART}, as YM90K^{PEG} weakly suppresses both weakly and strongly correlated cells (two-way ANOVA, main effect of YM90K^{PEG}, weakly correlated cells, $n = 48$, $p = 0.048$; strongly correlated cells, $n = 36$, $p = 0.004$; Figures S3C and S3D), and there is no significant continuous relationship between correlated variability and effects of YM90K^{PEG} (Figure S3E). These results suggest that the degree of recurrent excitation from pyramidal cells determines the recruitment of SST cells into the ISN and hint that there is functional heterogeneity among the population of SST cells that impacts their engagement in the ISN.

The effect of blocking AMPARs on SST cells depends on the behavioral state

We next investigated whether other conditions that increase excitation in the V1 cortical network would have a similar effect. Locomotion is well known to increase firing rates in V1.[27,38,39] To compare the same cells across behavioral states we examined the subset of SST and putative pyramidal cells, which could be measured at their preferred direction, in both stationary and running conditions, for all contrasts, and during both imaging sessions. Due to variation in animals' tendency for running, this led to the exclusion of two mice from both the YM90K^{DART} (n = 8 mice, 91 SST and 379 pyramidal cells; see method details) and YM90K^{PEG} (n = 4 mice, 54 SST and 275 pyramidal cells) experiments.

Consistent with previous reports, both SST (three-way ANOVA, main effect for locomotion, $p < 0.001$; Figures 5A–5C) and pyramidal cells ($p < 0.001$; Figures 5D–5F) are robustly facilitated by running.[27,39] Notably, locomotion dramatically changes the impact of YM90K^{DART} on SST cells (three-way ANOVA, YM90K^{DART} × locomotion interaction, $p = 0.024$; Figure 5C). The straightforward suppression observed at low contrast when the mice are stationary (paired t test with Bonferroni correction, $p = 0.003$; Figure 2B) no longer occurs when mice are running ($p = 0.794$; Figure 5A). At high contrast, the average

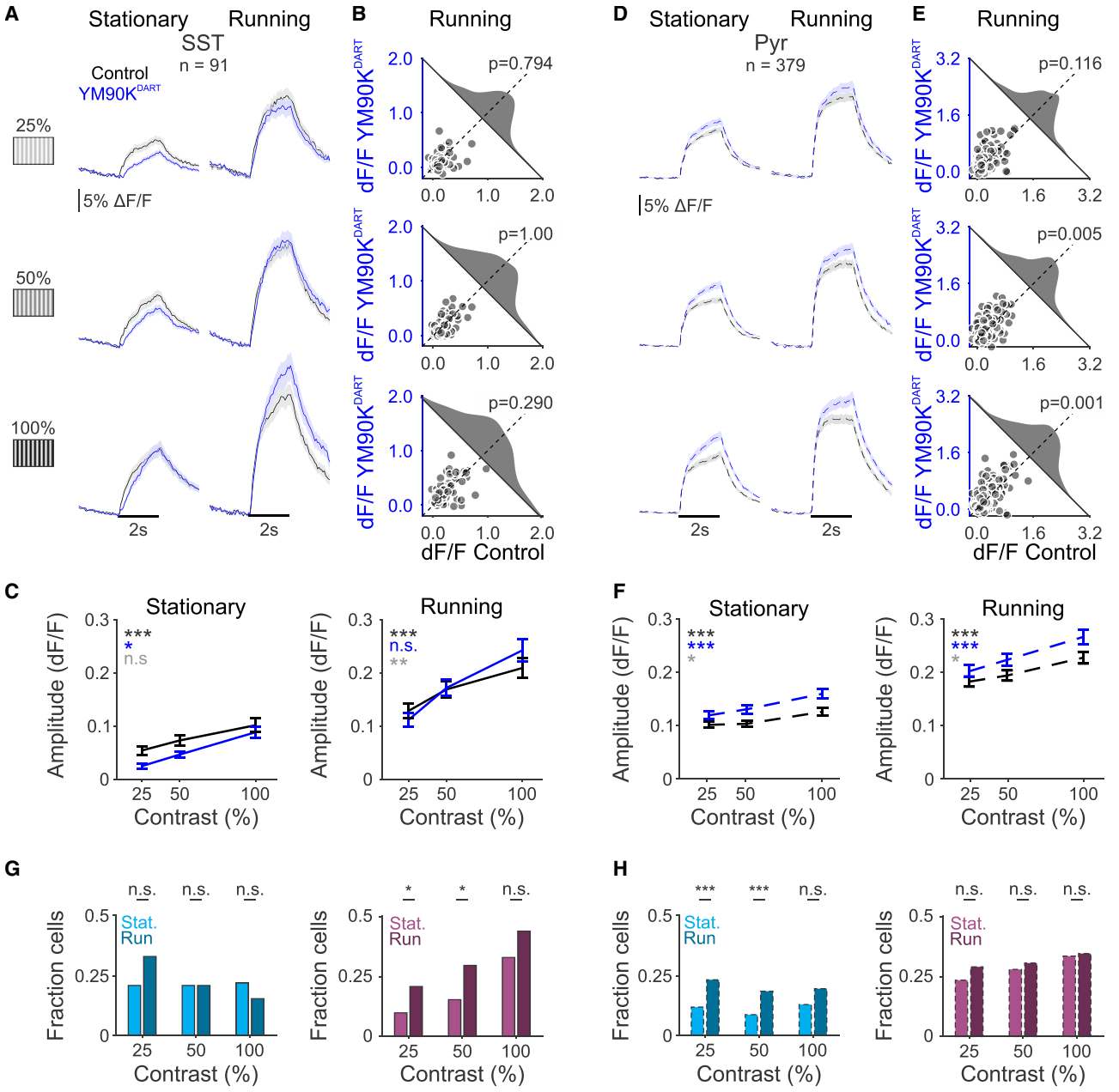

Figure 5. The effect of blocking AMPARs on SST cells depends on the behavioral state

(A) Grand average time courses for SST cells before (black) and after (blue) YM90K^{DART} during stationary (left) or running (right) epochs, at each contrast. All cells are matched across behavioral states and contrasts. Shaded error represents SEM across cells.

(B) Mean response during the stimulus period in control and after YM90K^{DART} for matched SST cells during running trials. Histogram is the probability distribution of ratios of responses in control and after YM90K^{DART}. Dashed line is unity line. *p* values are from paired t test.

(C) Mean response during stimulus period, for SST cells during stationary (left) or running (right) epochs, at each contrast. Error is SEM across cells. *p* values are from two-way ANOVA: main effect of contrast (black), drug (blue), and interaction (gray).

(D–F) Same as (A)–(C), for pyramidal cells.

(G) Fraction of SST cells suppressed (left, cyan) or facilitated (right, magenta) by more than 1 std of their control response during stationary (light) or running (dark) epochs. *p* values are from chi-squared test.

(H) Same as (G), for pyramidal cells. n.s., not significant; $^{*}p < 0.05$; $^{**}p < 0.01$; $^{***}p < 0.001$.

See also Figure S4.

response of SST cells trends toward the paradoxical elevation expected from inhibition stabilization, although this did not reach significance (p = 0.290). Mixed-effects models accounting for the nested data structure largely reproduce the results of the ANOVA (Tables S1C–S1E). An exception is that the interaction of YM90K^{DART} × locomotion is not significant in the mixed-effects model (p = 0.877; Table S1C). However, when stationary and running trials are modeled separately, the impact of YM90K^{DART} is isolated to the stationary trials (p = 0.004; Table S1D) and is not significant in the running trials (p = 0.103; Table S1E). Moreover, these effects are specific to the block of AMPARs on SST cells, as there is no dependence of the effects of YM90K^{PEG} on the behavioral state (three-way ANOVA, YM90K^{PEG} × locomotion interaction, p = 0.488; Figure S2).

The effects on the average responses are due to an increase in the fraction of SST cells facilitated by YM90K^{DART} when the mice are running (Bonferroni-corrected chi-square for stationary vs. running, 25% contrast, p = 0.040; 50% contrast, p = 0.021; 100% contrast p = 0.128; Figure 5G), without a significant difference in the fraction of cells suppressed ($p > 0.05$ for all contrasts). This variation in the direction of effects, with some SST cells being facilitated while others are suppressed, is consistent with our observation that SST cells are heterogeneous in their contributions to stabilizing the network.

Arousal has also been linked to network changes in visual cortex activity but is considered mechanistically distinct from locomotion.[40–42] To determine the impact of arousal on the network-stabilizing role of SST cells, we evaluated stationary trials and segregated them according to pupil diameter.[43,44] For each mouse, we measured pupil size during stationary epochs across both experimental days and performed a median split on the trials to assign them to large and small pupil categories (Figure S4A). We confirmed that the average pupil diameter is significantly greater in the large pupil trials (paired t test $p < 0.001$; Figure S4B) and is similar to the size during locomotion (paired t test, p = 0.079). To directly compare the same cells in each arousal state, we examined the subset of SST and putative pyramidal cells, which could be measured at their preferred direction, in both small and large pupil conditions, for all contrasts, and during both imaging sessions (n = 10 mice; 107 SST cells and 468 pyramidal cells).

Arousal slightly, but significantly, facilitates the responses of SST (three-way ANOVA, main effect for pupil size, p = 0.009) and pyramidal (three-way ANOVA, main effect for pupil size, $p < 0.001$) cells. As with locomotion, arousal alters the effect of YM90K^{DART} on SST cells (three-way ANOVA, YM90K^{DART} × pupil size interaction $p < 0.001$). Specifically, when mice are stationary, SST cells are suppressed by YM90K^{DART} during low-arousal trials (small-pupil trials: two-way ANOVA, main effect of YM90K^{DART}, $p < 0.001$; Figures S4D–S4G) but not during high-arousal trials (large-pupil trials: p = 0.150). This is consistent with the arousal-dependent effects of YM90K^{DART} on pyramidal cells (three-way ANOVA, YM90K^{DART} × pupil size interaction $p < 0.001$). Pyramidal cells are disinhibited during low arousal (small-pupil trials: two-way ANOVA, main effect of YM90K^{DART}, p = 0.011; Figures S4D–S4G) and even more so during high arousal (large-pupil trials: $p < 0.001$). These results suggest that recruitment of SST cells into the ISN is enhanced not only by stimulus strength but also by active states such as locomotion and arousal.

A theoretical framework for network stabilization by SST cells

To explore how input strength and arousal impact the recruitment of SST cells in stabilizing the network, we developed a model that includes the four major cortical neuron types: excitatory pyramidal cells (E) and three classes of inhibitory interneurons including SST (S), PV (P), and VIP (V) cells (Figure 6A$_i$). We used a mean-field approach, in which the average firing rate over all cells of a given type is represented by a time-varying scalar (e.g., r_E is the average firing rate over all E cells), and each cell type is described by a non-linear input-output transfer function, such as $r_E = \Phi_E(\sum synaptic\ input)$, which converts synaptic inputs to neural output, ensuring that neural activity cannot be negative. We eliminated six connections known to be weak from the literature[18,22,45] (I_S, W_{SP}, W_{SS}, W_{PV}, W_{EV} and W_{VV}).

To specifically interrogate the relationship between pyramidal and SST cells, we reduced the four-cell model to a two-cell model containing only E and S cells (Figure 6A$_{ii}$; see method details). This two-cell model has four effective synaptic weights, which incorporate the contributions of P and V cells. For instance, the connection from E to E has an effective synaptic weight of $W_{EE} - W_{EPE}$, where W_{EE} is the direct excitatory feedback loop from E to E, while W_{EPE} reflects an inhibitory feedback loop from E to P back to E (Figure S5). Critically, this allows us to account for the activity of P and V cells and their connectivity with S and E cells while constraining the parameter set to those informed by our empirical data. This is particularly relevant to the connectivity from S to P to E cells, which can reverse the sign of S cells' effect on E from inhibition to disinhibition, and the bidirectional connectivity between S and V cells, which provides mutual, potentially state-specific inhibition.

We then asked what dictates the effect of reducing excitation onto S cells (W_{SE}) in this network. For a given set of effective synaptic weights, the activity of E depends on the activity of S cells (the r_E nullcline; Figure 6B, dashed line) and vice versa (the r_S nullcline; Figure 6B, solid line). The intersection of these two lines yields the steady-state activity of E and S cells for the network. Manipulation of W_{SE} reduces the slope of the r_S nullcline (Figure 6B, blue line) and shifts E and S to a new steady-state firing rate. When the slope of the r_E nullcline is negative, decreasing excitation to S cells results in the expected decrease in S firing rates (Figure 6B$_i$). However, when the r_E nullcline slope is positive, the same manipulation can result in a paradoxical increase in S firing rates, the signature for their requirement for the ISN (Figure 6B$_{ii}$). Additionally, when the r_E nullcline slope is steeply positive, a different paradoxical effect emerges where both E and S rates decrease (Figure 6B$_{iii}$). Thus, the necessity of S cells for stabilization depends on the slope of the r_E nullcline.

The slope of the r_E nullcline depends on two key parameters: the net recurrent excitation among E cells ($\tilde{W}_{EE} = \Phi'_E W_{EE}$, where Φ'_E is the derivative of the E current-to-rate transfer function at the current rate) and the net inhibition of S to E ($\tilde{W}_{ES} = \Phi'_E W_{ES}$). This two-dimensional parameter space has five qualitatively discrete regions, which are defined by four lines: a non-ISN

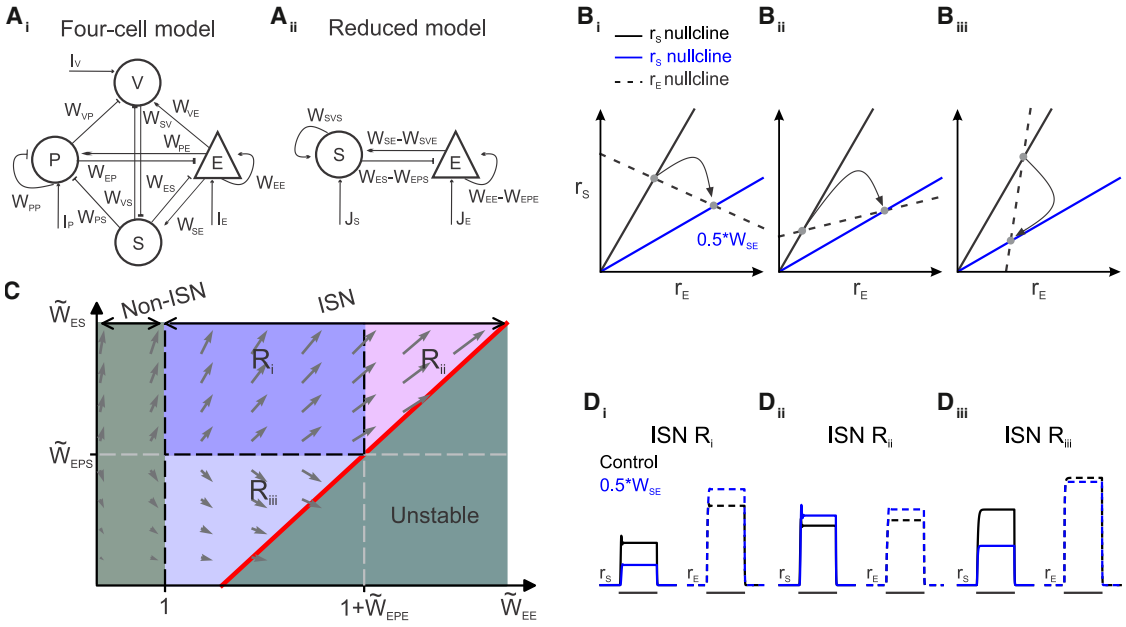

Figure 6. A theoretical framework for network stabilization by SST cells

(A) Schematic of the four-cell (left) and reduced two-cell (right) model.

($B_{i–iii}$) Schematic of r_E nullcline (dashed black), r_S nullcline in control (solid black), and r_S nullcline after a 50% reduction in W_{SE} (blue) when the slope of the r_E nullcline is negative (B_i), positive (B_{ii}), and steeply positive (B_{iii}). Arrows illustrate the shift in stability points (gray dots), and therefore the change in r_E and r_S after decrease in W_{SE}.

(C) Network stability in the space defined by $\tilde{W}_{EE}$ (effective recurrent excitation among E cells) and $\tilde{W}_{ES}$ (effective inhibition of S to E). Gray arrows illustrate how effective weights in $\tilde{W}_{EE} \times \tilde{W}_{ES}$ space change when stimulus intensity is increased.

($D_{i–iii}$) Simulated activity of pyramidal (dashed lines) and SST cells (solid lines) in response to a visual stimulus (thick black line) in each region of the space defined in (C) and corresponding to the nullclines illustrated in ($B_{i–iii}$).

See also Figure S5.

region, three distinct ISN regions ($R_{i–iii}$), and an unstable region (Figure 6C). The first line, $\tilde{W}_{EE} = 1$, determines whether the network is an ISN (when $\tilde{W}_{EE} > 1$) or not, i.e., excitation is weak enough to not require stabilization ($\tilde{W}_{EE} < 1$). The second line is $\tilde{W}_{EE} = 1 + \tilde{W}_{EPE}$, which determines whether the network can be stabilized by P cells alone (when $\tilde{W}_{EE} < 1 + \tilde{W}_{EPE}$). The third line is $\tilde{W}_{ES} = \tilde{W}_{EPS}$, where $\tilde{W}_{EPS}$ is the strength of S disinhibition of E cells via P (Figure S5), which determines whether the net inhibition by S cells outweighs their disinhibition (when $\tilde{W}_{ES} > \tilde{W}_{EPS}$). Finally, the fourth line defines the region in which the network is stable (see method details).

The first ISN region (R_i) is defined by three boundaries: $\tilde{W}_{EE} > 1$, $\tilde{W}_{EE} < 1 + \tilde{W}_{EPE}$, and $\tilde{W}_{ES} > \tilde{W}_{EPS}$. In this region, the network is an ISN, but P cells are sufficient to stabilize the network. In addition, the direct inhibition of E cells by S is stronger than the disinhibition through P cells. In this region, simulating a 0.5× decrease in excitation to S cells (W_{SE}), a conservative estimate of the efficacy of YM90K^{DART} based on our *in vitro* recordings, leads to the intuitively expected result, where S cells have reduced firing rates and E cells are disinhibited (Figure 6D_i).

Starting from region R_i, increasing $\tilde{W}_{EE}$ moves the network to the second ISN region (R_{ii}) when $\tilde{W}_{EE} > 1 + \tilde{W}_{EPE}$. In R_{ii}, P cells are no longer able to stabilize the network alone; thus, S cells are also needed for stability. This manifests in paradoxical effects of decreasing excitation onto S cells, where like E cells, they increase their firing rates (Figure 6D_{ii}). This region is bounded on the high end of $\tilde{W}_{EE}$ by an unstable region, with a boundary determined by $\tilde{W}_{ES}$. As $\tilde{W}_{ES}$ increases, S cells can stabilize more recurrent excitation, increasing the width of the region of $\tilde{W}_{EE}$ where S cells are necessary. A third ISN region (R_{iii}) occurs when $\tilde{W}_{ES} < \tilde{W}_{EPS}$. In R_{iii}, P cells can stabilize the network alone, but disinhibitory effects of S cells (via $\tilde{W}_{EPS}$) outweigh their direct inhibitory effect, such that removal of excitation from S cells reduces both S and E firing rates (Figure 6D_{iii}). Notably, these three ISN regions define when S cells are necessary, but not when they are sufficient, to stabilize the network (Figure S5).

Our model provides several potential explanations about how the network can transition between regions. First, given that the ISN regimes are defined by synaptic weights, short- and long-term mechanisms that alter synaptic weights,[20,39] such as behavioral state, could shift the network state. Second, even if the synaptic weights remain fixed, network state could be sensitive to input strength. This is because $\tilde{W}_{EE} = \Phi'_E W_{EE}$ becomes steeper as network activity increases because Φ_E is supralinear. Indeed, simulations of increasing visual stimulus strength move the network from R_i toward R_{ii} (Figure 6C, arrows). Thus, consistent with our data, our model supports the conclusion that SST cells are more likely to be engaged in the ISN with increasing stimulus contrast.

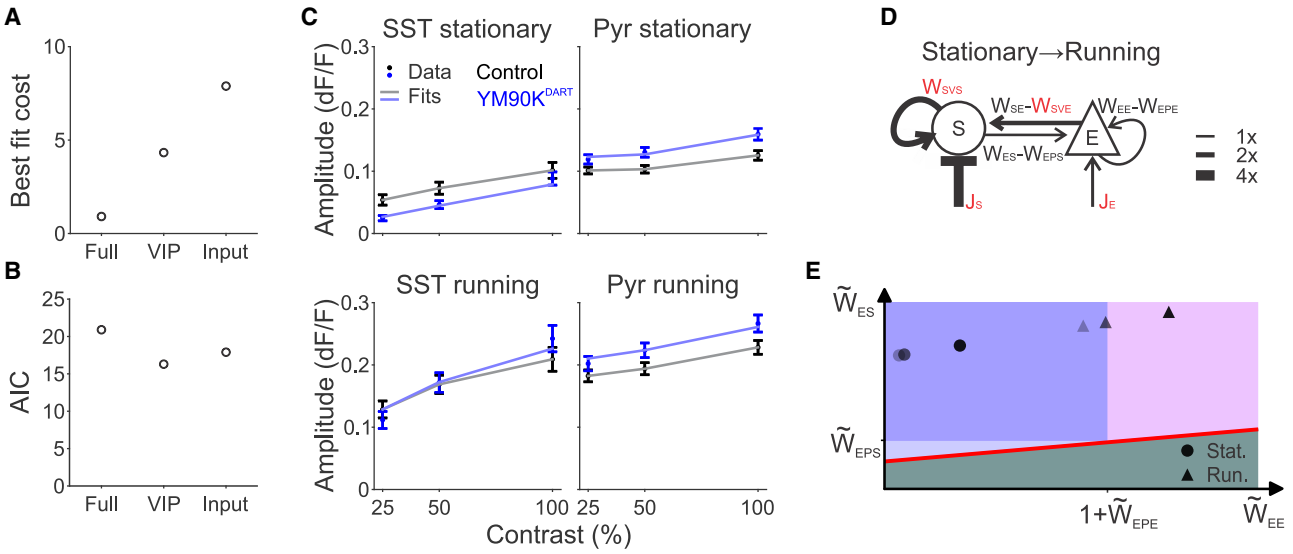

Figure 7. Paradoxical effects indicate the necessity of SST cells for network stabilization

(A) Cost of the best fit for each model.

(B) Akaike information criterion (AIC) values for each model.

(C) Empirical (dark data points, mean ± SEM from Figures 5B–5D) and simulated (light lines) responses of SST (left) and pyramidal (right) cells to increasing contrast, in stationary (top) or locomotion (bottom) states in control (gray) and after YM90K^{DART} (light blue).

(D) Schematic of changes to weights to fit changes from stationary to running. Weights in red can change across state in the VIP model. Line thickness is proportional to weight change.

(E) Position of model best fit parameters at each contrast (shading) and behavioral state (circles, stationary; triangles, running) in the phase space from Figure 5. Instability line (red) corresponds to the high-contrast, running condition.

See also Figure S6.

Stimulus strength and behavioral state recruit SST cells into the ISN through distinct effects on the network

To quantitatively investigate how changing stimulus strength and behavioral state may act to engage SST cells into network stabilization, we fit our model weights to the neural responses in control and YM90K^{DART}. In our model, YM90K^{DART} solely affects W_{SE} (since we assume that the direct sensory input to S cells [I_S] is negligible[22]) and is modeled as a fractional change of this weight, $(1-x)W_{SE}$ with x set to 0.5 (Figure S6). We modeled changes in contrast by changing the external inputs, J_E and J_S. To model changes in the behavioral state, we allowed both external inputs and weights to vary, capturing effects on both the strength of feedforward excitation and the synaptic connectivity within the network.[39,46]

When all weights are allowed to vary between stationary and running conditions, the model can quantitatively fit the data very well ("full model," Figures 7A and S6; Table S3). Multiple studies have emphasized the role of VIP cells in regulating SST cell activity[24,25] and as a mechanism for locomotion modulation.[26] To test a model in which only the external inputs and the gain of V cells were permitted to change between behavioral states, we fit a gain term g that was applied to W_{SVS} and W_{SVE}, with all other weights fixed. This model successfully fits the data ("VIP model," Figures 7A–7C; Table S4) and produces a lower Akaike information criterion (AIC)[47] value than the full model (Figure 7B). Conversely, a model where only external inputs could vary between states ("input model") results in a higher cost and AIC value than the VIP model (Figures 7A, 7B, and S6; Table S5). Thus, we focused on the VIP model since it yields the best fit according to AIC.

The contrast-dependent effects of YM90K^{DART} on pyramidal and SST cells within each state are captured by changes in the net inputs J_E and J_S (Figure 7C; Table S4). J_E is positive and increases with contrast, consistent with increasing feedforward input. In comparison, J_S is always negative, reflecting increased inhibition to S cells from V cells, as our model includes no direct sensory input to S (Figure S5). Additionally, J_S decreases with contrast, consistent with increased input to V cells with increasing stimulus strength.

Our reduced model incorporates the activity and connections of V and P cells in relation to S and E cells. Given that VIP interneurons have bidirectional inhibition with SST interneurons and are robustly activated by locomotion,[18,26,27,39] the role of V cells and their mutual connectivity with S cells are particularly relevant to understanding how locomotion regulates the incorporation of S cells into the ISN. In the transition from the stationary to locomotion states, the increased gain to V cells increases W_{SVS} such that the net recurrent effect of S cells through V cells is more excitatory (Figure 7D; Table S4). Meanwhile, W_{SVE} becomes more negative, such that $W_{SE} - W_{SVE}$, the net excitation from E to S cells, also increases. Finally, the external input to E cells (J_E) is elevated during locomotion. Thus, despite the decrease in J_S, the net effects combine to increase recurrent excitation of S cells alongside higher activity of E cells during locomotion.

Plotting the fitted network in the $\tilde{W}_{EE}$ vs. $\tilde{W}_{ES}$ space reveals how the network moves as a function of input strength and

behavioral state (Figure 7E). The network is in R_i (in which S cells are not required for stability) in stationary conditions. As contrast increases, the network moves toward the boundary between R_i and R_{ii}, that is, the effective recurrent excitation approaches the value at which it can no longer be stabilized by PV cells alone. Running shifts the network closer still to the R_i-R_{ii} boundary, and when running coincides with high contrast, the network crosses the border into R_{ii}. Thus, high-contrast stimuli during active epochs produce a network state in which P cells are insufficient to balance the effective recurrent excitation of pyramidal cells, and S cells are required to prevent network instability. We also find that the strength of inhibition of S cells onto pyramidal cells exceeds the disinhibition they provide through P cells.

The model supports our interpretation that YM90K^{DART} reveals the conditions under which SST cells contribute to the ISN and that distinct mechanisms underlie the recruitment of SST cells to the ISN with increasing contrast or locomotion. Specifically, while contrast alters network activity directly through increased feedforward input, running additionally changes the local interactions within V1, potentially via its action on VIP cells.

Differential requirement of SST and PV cells for network stability

If SST cells are required for network stability under conditions of strong sensory input and high arousal as our model indicates, this suggests that strongly suppressing SST cells should produce runaway excitation selectively under these conditions. We simulated optogenetic hyperpolarization of S cells in our V1 network model and assessed the effect on the firing rate of E cells (r_E). This manipulation leads to elevated, but stable, r_E during the low-contrast stationary condition but produces runaway excitation in the high-contrast running condition (Figure S7A). Notably, even when visual input and arousal are high, weak suppression of SST cells can be overcome by increased recurrent excitation and does not produce runaway excitation. Only when SST cells' output is completely silenced does the network become unstable. In comparison, even partial suppression of P cells produces nearly immediate runaway excitation regardless of contrast or behavioral state (Figure S7B). Thus, while S cells are required for the ISN under specific conditions, P cells are required under all conditions.

To test these model predictions *in vivo*, we used PV::Cre mice to express HTP on PV cells and performed two-photon calcium imaging during passive presentation of drifting gratings before and after YM90K^{DART} infusion (n = 3 mice). This manipulation evokes strong, sporadic, highly synchronized network events that were not present in the baseline condition (Video S1 and S2). This results in an increase in both sample entropy of the cumulative population activity (paired t test, p = 0.026; Figure S7C) and synchrony across the network (p = 0.015; Figure S7D). In comparison, infusion of YM90K^{PEG} in PV::Cre mice (n = 2; Video S3) or YM90K^{DART} in SST::Cre mice (n = 3; Video S4) had significantly less change (post/pre) in either sample entropy (unpaired t test with correction for multiple comparisons: PV + YM90K^{DART} vs. PV + YM90K^{PEG}, p = 0.045; PV + YM90K^{DART} vs. SST + YM90K^{DART}, p = 0.041; Figure S7C) or synchrony (PV + YM90K^{DART} vs. PV + YM90K^{PEG}, p = 0.004; PV + YM90K^{DART} vs. SST + YM90K^{DART}, p = 0.005; Figure S7D). Together, these simulated and *in vivo* findings highlight the distinct roles of SST and PV cells in network stabilization.

DISCUSSION

ISNs are proposed to enable sensory cortex to normalize responses across a broad range of contexts.[6,32–34] We reveal that SST cells are selectively required for network stabilization in mouse V1 under high sensory drive and active behavioral states, providing a concrete example of how the diverse cell types in the V1 enable this flexibility.

Cell-type-specific pharmacology for probing the necessity of SST cells in stabilization

These experiments were enabled by the ability to selectively block synaptic excitation onto SST cells by using the AMPAR antagonist YM90K^{DART}, allowing us to directly manipulate the recurrent excitation from pyramidal to SST cells (W_{SE}). When mice are quiescent and visual stimuli are weak, YM90K^{DART} reduces SST cells' responses, while moderately disinhibiting responses of putative pyramidal cells. This intuitive effect is consistent with past work highlighting the role of PV cells, rather than SST cells, in network stabilization.[5,10,13,14,16] However, our model and other models[20] suggest that there is a limit to the strength of recurrent excitation that PV cells alone can stabilize and that, past this point, SST cells are also needed for network stabilization. Indeed, when visual stimuli are strong, decreasing excitation onto SST cells elicits stronger disinhibition of excitatory cells and a paradoxical facilitation of an increasing number of SST cells. Our model recapitulates the contrast-dependent effects of YM90K^{DART} on both pyramidal and SST cells solely through changes in the sensory inputs to these cell types (J_E and J_S). In our model, contrast-dependent effects arise due to a non-linearity of the input-output transfer function, but other non-linearities, such as those introduced by short-term plasticity, could also play a role.

Notably, the paradoxical facilitation of SST cells is contingent on some remaining excitatory input, potentially mediated by a subset of unblocked AMPARs. Our *in vitro* electrophysiology recordings demonstrate substantial, but not complete, reduction of AMPAR-mediated excitation on SST cells. Excitatory input to SST cells is facilitating and thus may be more effectively recruited by the higher frequency firing evoked with increasing stimulus strength.[23,48] Alternatively, NMDA, kainate, and metabotropic glutamate receptors[49–52] may also preserve excitatory drive under YM90K^{DART}.

Circuit mechanisms for engagement of SST cells in network stabilization

Our finding that the effect of YM90K^{DART} depends on each SST cell's correlation with local pyramidal activity supports our conclusion that we are revealing ISN engagement. In an ISN, strongly coupled cells should be facilitated by the disinhibitory effects of YM90K^{DART}, whereas weakly coupled neurons undergo net suppression. Future experiments probing molecularly distinct subtypes of SST cells will be helpful in understanding the origins of this heterogeneity. These results suggest a gradual transition from a purely PV-stabilized network to an

SST-stabilized network, with the progressively stronger recruitment of SST cells into the ISN.

Behavioral state critically controls the recruitment of SST cells into the ISN. Locomotion dramatically increases stimulus responses of all major cell types in the V1 circuit,[27,38,39] and models suggest that visual stimulation coupled with locomotion creates the conditions for SST recruitment to the ISN.[20,21] Indeed, when mice are running, we find limited suppression of SST cells by YM90K^{DART} even with low-contrast stimuli. When the mice run during high-contrast stimuli, we observe clear paradoxical facilitation. Arousal and locomotion are associated with neuromodulation of V1, including cholinergic and noradrenergic inputs.[26,53,54] By altering cells' excitability and synaptic output, neuromodulation could effectively change the connectivity weights in the V1 circuit,[39] driving the requirement of SST cells for stabilization. Consistent with the literature, our model suggests that the effect of locomotion may occur through the modulation of VIP cells.[26] Of note, both SST cells and VIP cells are modulated by stimulus size: whereas SST cells prefer larger stimuli, VIP cells prefer smaller stimuli.[25,39] Thus, the size of the visual stimulus may further alter the interaction between SST and VIP cells and therefore the recruitment of SST cells to the ISN, particularly during aroused behavioral states.

Contrary to our finding of SST necessity for stabilization, optogenetic suppression of SST cells has not resulted in epilepsy.[9,55] Our simulated optogenetic suppression in the model V1 network demonstrates several potential reasons for this apparent discrepancy. First, because SST cells are only recruited to the ISN when sensory input and arousal are both high, optogenetic suppression of SST cells during weaker sensory input or low arousal states does not destabilize the network. Additionally, even during conditions of high contrast and locomotion, incomplete suppression of SST cells—which is most likely the case for typical experimental applications—is insufficient to drive runaway excitation. Finally, while complete silencing of SST cells does yield runaway excitation during high contrast coupled with locomotion in our V1 model, this network state evolves over several hundred milliseconds after coincident onset of SST suppression and the visual stimulus. Thus, brief visual stimuli or delayed optogenetic suppression beginning after the strong initial portion of the visual stimulus response[9,55] is likely to be insufficient to drive epilepsy. Therefore, we believe that past experimental manipulations have not truly achieved the conditions required to produce epileptic activity through SST suppression and that these results are not contradictory to the present findings.

Limitations of the study

These experiments employed the high-affinity indicator GCaMP8s, which has sensitive single-action-potential detection[56] but may saturate under higher levels of activity. Thus, we may underestimate the degree of disinhibition in the network. Indeed, we observe less disinhibition of putative pyramidal cells following YM90K^{DART} during locomotion, potentially due to the non-linearities of the indicator. While we accounted for the spike-to-calcium conversion in our model fits, these non-linearities may nonetheless distort the input-output functions and our weight estimates. Notably, these weight estimates are only constrained by data from SST and putative pyramidal cells. As a result, these data are only able to constrain composite connectivity parameters and not the full 4×4 weight matrix. Due to the lack of data on PV and VIP cells, we had to make an assumption on their transfer function, which we took for simplicity to be threshold-linear. Future experiments monitoring these populations will lead to a more complete network model, with its full 4×4 weight matrix.

Conclusions and future directions

While SST cells' recruitment into the ISN during the presentation of strong sensory stimuli and states of behavioral arousal is likely general across sensory cortex, the conditions that determine the transition between states will depend on the specific architecture of each cortical area. As the density of different cell types and their connectivity vary across the cortex,[57,58] so will the boundaries between ISN regions. An important question for future inquiry is how the transition from a purely PV-stabilized to a PV-and-SST-stabilized network impacts sensory processing. This transition may have little effect on the input-output function of the excitatory population and simply enable the network to maintain stability across a broader range of contexts. Alternatively, the transition to reliance upon dendrite-targeting SST cells may alter the dynamics of synaptic integration[59–61] and plasticity[62] and may be finely tuned within each cortical area.[57,58] Synapse- and cell-type-specific pharmacology coupled with our modeling framework promise to reveal how each node in the cortical circuit supports sensory processing across a broad range of environmental and behavioral contexts.

RESOURCE AVAILABILITY

Lead contact

Further information and requests for resources and reagents should be directed to the lead contact, Lindsey Glickfeld (glickfeld@neuro.duke.edu).

Materials availability

No new reagents were generated as a result of this study.

Data and code availability

- All data and code needed to generate the manuscript figures have been deposited on Figshare and is available as of the date of publication. Accession numbers are listed in the key resources table.
- All original code needed to generate model has been deposited on GitHub and is available as of the date of publication. Accession numbers are listed in the key resources table.
- Any additional information required to reanalyze the data reported in this paper is available from the lead contact upon request.

ACKNOWLEDGMENTS

We thank Wenjuan Kong, Lou Campillo, Lindsey Wilson, T.J. Wagner, Gloria Kim, Dr. Sasha Burwell, and Megan Stone for assistance with husbandry, surgeries, retinotopic mapping, and histology. We thank Dr. Ashley Wilson for initial characterization of DART delivery and expression in V1, Dr. Mark Histed for the gift of a virus for expression of GCaMP8s, Dr. Kevin Franks for the use of his epifluorescence microscope, and Dr. Yuansi Chen for advice on statistical

approaches. We thank Dr. Court Hull for assistance with measuring the effect of YM90K^{DART} in response to high-frequency trains and comments on the manuscript. We thank Dr. Rich Mooney and members of the Hull and Glickfeld labs for insight throughout the project. This work was supported by grants from the National Institutes of Health (R01-EY031716 to L.L.G., F32-EY034013 to C.M.C., F31-EY031941 to J.Y.L., and RF1-MH117055, DP2-MH1194025, R01-NS107472, and R61-DA051530 to M.R.T.), the American Heart Association (to S.S.X.L.), and the Holland-Trice Foundation (to L.L.G.).

AUTHOR CONTRIBUTIONS

Conceptualization, C.M.C., N.B., M.R.T., and L.L.G.; methodology, C.M.C., T.H., B.C.S., and S.S.X.L.; investigation and data curation, C.M.C., J.Y.L., and T.H.; formal analysis, C.M.C., Y.P., D.S.A., J.Y.L., T.H., and L.L.G.; writing – original draft, C.M.C. and L.L.G.; writing – review and editing, C.M.C., J.Y.L., N.B., M.R.T., and L.L.G.; visualization, C.M.C., Y.P., T.H., and L.L.G.; supervision, C.M.C., N.B., M.R.T., and L.L.G.; funding acquisition, C.M.C., M.R.T., and L.L.G.

DECLARATION OF INTERESTS

M.R.T. and B.C.S. are on a patent application describing HTL.2 and its applications.

STAR★METHODS

Detailed methods are provided in the online version of this paper and include the following:

- KEY RESOURCES TABLE
- EXPERIMENTAL MODEL AND SUBJECT DETAILS
- METHOD DETAILS
  - Surgical procedures
  - Experimental procedures
- QUANTIFICATION AND STATISTICAL ANALYSIS
  - Electrophysiology
  - Two-photon calcium imaging
  - Computational modeling

SUPPLEMENTAL INFORMATION

Supplemental information can be found online at https://doi.org/10.1016/j.celrep.2025.115954.

Received: December 1, 2024
Revised: May 7, 2025
Accepted: June 12, 2025
Published: July 9, 2025

REFERENCES

1. Heeger, D.J. (1992). Normalization of cell responses in cat striate cortex. Vis. Neurosci. *9*, 181–197.
2. Carandini, M., and Heeger, D.J. (2011). Normalization as a canonical neural computation. Nat. Rev. Neurosci. *13*, 51–62.
3. Carandini, M., Heeger, D.J., and Movshon, J.A. (1997). Linearity and normalization in simple cells of the macaque primary visual cortex. J. Neurosci. *17*, 8621–8644.
4. Litwin-Kumar, A., Rosenbaum, R., and Doiron, B. (2016). Inhibitory stabilization and visual coding in cortical circuits with multiple interneuron subtypes. J. Neurophysiol. *115*, 1399–1409.
5. Palmigiano, A., Fumarola, F., Mossing, D.P., Kraynyukova, N., Adesnik, H., and Miller, K.D. (2020). Common rules underlying optogenetic and behavioral modulation of responses in multi-cell-type V1 circuits. bioRxiv *11.11*, 378729. https://doi.org/10.1101/2020.11.11.378729.
6. Tsodyks, M.V., Skaggs, W.E., Sejnowski, T.J., and McNaughton, B.L. (1997). Paradoxical effects of external modulation of inhibitory interneurons. J. Neurosci. *17*, 4382–4388.
7. Ozeki, H., Finn, I.M., Schaffer, E.S., Miller, K.D., and Ferster, D. (2009). Inhibitory stabilization of the cortical network underlies visual surround suppression. Neuron *62*, 578–592.
8. Kato, H.K., Asinof, S.K., and Isaacson, J.S. (2017). Network-Level Control of Frequency Tuning in Auditory Cortex. Neuron *95*, 412–423.
9. Adesnik, H. (2017). Synaptic Mechanisms of Feature Coding in the Visual Cortex of Awake Mice. Neuron *95*, 1147–1159.
10. Sanzeni, A., Akitake, B., Goldbach, H.C., Leedy, C.E., Brunel, N., and Histed, M.H. (2020). Inhibition stabilization is a widespread property of cortical networks. eLife *9*, e54875.
11. Millman, D.J., Ocker, G.K., Caldejon, S., Kato, I., Larkin, J.D., Lee, E.K., Luviano, J., Nayan, C., Nguyen, T.V., North, K., et al. (2020). VIP interneurons in mouse primary visual cortex selectively enhance responses to weak but specific stimuli. eLife *9*, e55130.
12. Liu, L.D., Miller, K.D., and Pack, C.C. (2018). A Unifying Motif for Spatial and Directional Surround Suppression. J. Neurosci. *38*, 989–999.
13. Li, N., Chen, S., Guo, Z.V., Chen, H., Huo, Y., Inagaki, H.K., Chen, G., Davis, C., Hansel, D., Guo, C., and Svoboda, K. (2019). Spatiotemporal constraints on optogenetic inactivation in cortical circuits. eLife *8*, e48622.
14. Moore, A.K., Weible, A.P., Balmer, T.S., Trussell, L.O., and Wehr, M. (2018). Rapid Rebalancing of Excitation and Inhibition by Cortical Circuitry. Neuron *97*, 1341–1355.
15. Sato, T.K., Haider, B., Häusser, M., and Carandini, M. (2016). An excitatory basis for divisive normalization in visual cortex. Nat. Neurosci. *19*, 568–570.
16. Romero-Sosa, J.L., Motanis, H., and Buonomano, D.V. (2021). Differential Excitability of PV and SST Neurons Results in Distinct Functional Roles in Inhibition Stabilization of Up States. J. Neurosci. *41*, 7182–7196.
17. Jiang, X., Shen, S., Cadwell, C.R., Berens, P., Sinz, F., Ecker, A.S., Patel, S., and Tolias, A.S. (2015). Principles of connectivity among morphologically defined cell types in adult neocortex. Science *350*, aac9462.
18. Pfeffer, C.K., Xue, M., He, M., Huang, Z.J., and Scanziani, M. (2013). Inhibition of inhibition in visual cortex: the logic of connections between molecularly distinct interneurons. Nat. Neurosci. *16*, 1068–1076.
19. Tremblay, R., Lee, S., and Rudy, B. (2016). GABAergic Interneurons in the Neocortex: From Cellular Properties to Circuits. Neuron *91*, 260–292.
20. Waitzmann, F., Wu, Y.K., and Gjorgjieva, J. (2024). Top-down modulation in canonical cortical circuits with short-term plasticity. Proc. Natl. Acad. Sci. USA *121*, e2311040121.
21. Garcia Del Molino, L.C., Yang, G.R., Mejias, J.F., and Wang, X.-J. (2017). Paradoxical response reversal of top-down modulation in cortical circuits with three interneuron types. eLife *6*, e29742.
22. Adesnik, H., Bruns, W., Taniguchi, H., Huang, Z.J., and Scanziani, M. (2012). A neural circuit for spatial summation in visual cortex. Nature *490*, 226–231.
23. Kapfer, C., Glickfeld, L.L., Atallah, B.V., and Scanziani, M. (2007). Supralinear increase of recurrent inhibition during sparse activity in the somatosensory cortex. Nat. Neurosci. *10*, 743–753.
24. Keller, A.J., Dipoppa, M., Roth, M.M., Caudill, M.S., Ingrosso, A., Miller, K.D., and Scanziani, M. (2020). A Disinhibitory Circuit for Contextual Modulation in Primary Visual Cortex. Neuron *108*, 1181–1193.
25. Mossing, D.P., Veit, J., Palmigiano, A., Miller, K.D., and Adesnik, H. (2021). Antagonistic inhibitory subnetworks control cooperation and competition

across cortical space. Preprint at bioRxiv. https://doi.org/10.1101/2021.03.31.437953.

26. Fu, Y., Tucciarone, J.M., Espinosa, J.S., Sheng, N., Darcy, D.P., Nicoll, R.A., Huang, Z.J., and Stryker, M.P. (2014). A cortical circuit for gain control by behavioral state. Cell *156*, 1139–1152.
27. Pakan, J.M., Lowe, S.C., Dylda, E., Keemink, S.W., Currie, S.P., Coutts, C.A., and Rochefort, N.L. (2016). Behavioral-state modulation of inhibition is context-dependent and cell type specific in mouse visual cortex. eLife *5*. e14985–18.
28. Shields, B.C., Kahuno, E., Kim, C., Apostolides, P.F., Brown, J., Lindo, S., Mensh, B.D., Dudman, J.T., Lavis, L.D., and Tadross, M.R. (2017). Deconstructing behavioral neuropharmacology with cellular specificity. Science *356*, eaaj2161.
29. Shields, B.C., Yan, H., Lim, S.S.X., Burwell, S.C.V., Cammarata, C.M., Fleming, E.A., Yousefzadeh, S.A., Goldenshtein, V.Z., Kahuno, E.W., Vagadia, P.P., et al. (2024). DART.2: bidirectional synaptic pharmacology with thousandfold cellular specificity. Nat. Methods *21*, 1288–1297.
30. Marks, T.D., and Goard, M.J. (2021). Stimulus-dependent representational drift in primary visual cortex. Nat. Commun. *12*, 5169.
31. Sadeh, S., and Clopath, C. (2022). Contribution of behavioural variability to representational drift. eLife *11*, e77907.
32. van Vreeswijk, C., and Sompolinsky, H. (1998). Chaotic balanced state in a model of cortical circuits. Neural Comput. *10*, 1321–1371.
33. Rubin, D.B., Van Hooser, S.D., and Miller, K.D. (2015). The stabilized supralinear network: a unifying circuit motif underlying multi-input integration in sensory cortex. Neuron *85*, 402–417.
34. Murphy, B.K., and Miller, K.D. (2009). Balanced amplification: a new mechanism of selective amplification of neural activity patterns. Neuron *61*, 635–648.
35. Okun, M., Steinmetz, N., Cossell, L., Iacaruso, M.F., Ko, H., Barthó, P., Moore, T., Hofer, S.B., Mrsic-Flogel, T.D., Carandini, M., and Harris, K.D. (2015). Diverse coupling of neurons to populations in sensory cortex. Nature *521*, 511–515.
36. Cohen, M.R., and Kohn, A. (2011). Measuring and interpreting neuronal correlations. Nat. Neurosci. *14*, 811–819.
37. Thiele, A., Herrero, J.L., Distler, C., and Hoffmann, K.-P. (2012). Contribution of cholinergic and GABAergic mechanisms to direction tuning, discriminability, response reliability, and neuronal rate correlations in macaque middle temporal area. J. Neurosci. *32*, 16602–16615.
38. Niell, C.M., and Stryker, M.P. (2010). Modulation of Visual Responses by Behavioral State in Mouse Visual Cortex. Neuron *65*, 472–479.
39. Dipoppa, M., Ranson, A., Krumin, M., Pachitariu, M., Carandini, M., and Harris, K.D. (2018). Vision and Locomotion Shape the Interactions between Neuron Types in Mouse Visual Cortex. Neuron *98*, 602–615.
40. Vinck, M., Batista-Brito, R., Knoblich, U., and Cardin, J.A. (2015). Arousal and locomotion make distinct contributions to cortical activity patterns and visual encoding. Neuron *86*, 740–754.
41. Larsen, R.S., and Waters, J. (2018). Neuromodulatory Correlates of Pupil Dilation. Front. Neural Circuits *12*, 21.
42. Reimer, J., McGinley, M.J., Liu, Y., Rodenkirch, C., Wang, Q., McCormick, D.A., and Tolias, A.S. (2016). Pupil fluctuations track rapid changes in adrenergic and cholinergic activity in cortex. Nat. Commun. *7*, 13289.
43. Reimer, J., Froudarakis, E., Cadwell, C.R., Yatsenko, D., Denfield, G.H., and Tolias, A.S. (2014). Pupil Fluctuations Track Fast Switching of Cortical States during Quiet Wakefulness. Neuron *84*, 355–362.
44. Gilzenrat, M.S., Nieuwenhuis, S., Jepma, M., and Cohen, J.D. (2010). Pupil diameter tracks changes in control state predicted by the adaptive gain theory of locus coeruleus function. Cogn. Affect. Behav. Neurosci. *10*, 252–269.
45. Campagnola, L., Seeman, S.C., Chartrand, T., Kim, L., Hoggarth, A., Gamlin, C., Ito, S., Trinh, J., Davoudian, P., Radaelli, C., et al. (2022). Local connectivity and synaptic dynamics in mouse and human neocortex. Science *375*, eabj5861.
46. Aydın, Ç., Couto, J., Giugliano, M., Farrow, K., and Bonin, V. (2018). Locomotion modulates specific functional cell types in the mouse visual thalamus. Nat. Commun. *9*, 4882.
47. Akaike, H. (1974). A new look at the statistical model identification. IEEE Trans. Automat. Contr. *19*, 716–723.
48. Silberberg, G., and Markram, H. (2007). Disynaptic inhibition between neocortical pyramidal cells mediated by Martinotti cells. Neuron *53*, 735–746.
49. Booker, S.A., and Wyllie, D.J.A. (2021). NMDA receptor function in inhibitory neurons. Neuropharmacology *196*, 108609.
50. Kroon, T., Dawitz, J., Kramvis, I., Anink, J., Obermayer, J., Verhoog, M.B., Wilbers, R., Goriounova, N.A., Idema, S., Baayen, J.C., et al. (2019). Group I mGluR-mediated activation of Martinotti cells inhibits local cortical circuitry in human cortex. Front. Cell. Neurosci. *13*, 315.
51. Dwivedi, D., Dumontier, D., Sherer, M., Lin, S., Mirow, A.M.C., Qiu, Y., Xu, Q., Liebman, S.A., Joseph, D., Datta, S.R., et al. (2024). Metabotropic signaling within somatostatin interneurons controls transient thalamocortical inputs during development. Nat. Commun. *15*, 5421.
52. Selvakumar, P., Lee, J., Khanra, N., He, C., Munguba, H., Kiese, L., Broichhagen, J., Reiner, A., Levitz, J., and Meyerson, J.R. (2021). Structural and compositional diversity in the kainate receptor family. Cell Rep. *37*, 109891.
53. Larsen, R.S., Turschak, E., Daigle, T., Zeng, H., Zhuang, J., and Waters, J. (2018). Activation of neuromodulatory axon projections in primary visual cortex during periods of locomotion and pupil dilation. Preprint at bioRxiv. https://doi.org/10.1101/502013.
54. Polack, P.O., Friedman, J., and Golshani, P. (2013). Cellular mechanisms of brain state-dependent gain modulation in visual cortex. Nat. Neurosci. *16*, 1331–1339.
55. Veit, J., Hakim, R., Jadi, M.P., Sejnowski, T.J., and Adesnik, H. (2017). Cortical gamma band synchronization through somatostatin interneurons. Nat. Neurosci. *20*, 951–959.
56. Zhang, Y., Rózsa, M., Liang, Y., Bushey, D., Wei, Z., Zheng, J., Reep, D., Broussard, G.J., Tsang, A., Tsegaye, G., et al. (2023). Fast and sensitive GCaMP calcium indicators for imaging neural populations. Nature *615*, 884–891.
57. Li, J.Y., Hass, C.A., Matthews, I., Kristl, A.C., and Glickfeld, L.L. (2021). Distinct recruitment of feedforward and recurrent pathways across higher-order areas of mouse visual cortex. Curr. Biol. *31*, 5024–5036.
58. Kim, Y., Yang, G.R., Pradhan, K., Venkataraju, K.U., Bota, M., García Del Molino, L.C., Fitzgerald, G., Ram, K., He, M., Levine, J.M., et al. (2017). Brain-wide Maps Reveal Stereotyped Cell-Type-Based Cortical Architecture and Subcortical Sexual Dimorphism. Cell *171*, 456–469.
59. Dorsett, C., Philpot, B.D., Smith, S.L., and Smith, I.T. (2021). The Impact of SST and PV Interneurons on Nonlinear Synaptic Integration in the Neocortex. eNeuro *8*.
60. Pouille, F., and Scanziani, M. (2004). Routing of spike series by dynamic circuits in the hippocampus. Nature *429*, 717–723.
61. Pouille, F., Watkinson, O., Scanziani, M., and Trevelyan, A.J. (2013). The contribution of synaptic location to inhibitory gain control in pyramidal cells. Physiol. Rep. *1*, e00067.
62. Chiu, C.Q., Lur, G., Morse, T.M., Carnevale, N.T., Ellis-Davies, G.C.R., and Higley, M.J. (2013). Compartmentalization of GABAergic inhibition by dendritic spines. Science *340*, 759–762.
63. Ferguson, K.A., Salameh, J., Alba, C., Selwyn, H., Barnes, C., Lohani, S., and Cardin, J.A. (2023). VIP interneurons regulate cortical size tuning and visual perception. Cell Rep. *42*, 113088.

64. Jin, M., Beck, J.M., and Glickfeld, L.L. (2019). Neuronal adaptation reveals a suboptimal decoding of orientation tuned populations in the mouse visual cortex. J. Neurosci. *39*, 3867–3881.

65. Chen, N., Sugihara, H., and Sur, M. (2015). An acetylcholine-activated microcircuit drives temporal dynamics of cortical activity. Nat. Neurosci. *18*, 892–902.

66. Khoury, C.F., Fala, N.G., and Runyan, C.A. (2023). Arousal and locomotion differently modulate activity of somatostatin neurons across cortex. eNeuro *10*.

67. Andermann, M.L., Kerlin, A.M., Roumis, D.K., Glickfeld, L.L., and Reid, R. C. (2011). Functional specialization of mouse higher visual cortical areas. Neuron *72*, 1025–1039.

STAR★METHODS

KEY RESOURCES TABLE

REAGENT or RESOURCE	SOURCE	IDENTIFIER
Bacterial and virus strains		
AAV9-pGP-AAV-*syn*-jGCaMP8s-WPRE	Gift from Mark Histed, NIH	Addgene: 162374
AAV10-pGP-AAV-*syn*-jGCaMP8s-WPRE	VectorBuilder	Addgene: 162374
AAV9-pGP-*syn*-jGCaMP8f-WPRE	Addgene	Addgene: v201514
AAV10 CAG-CreON_WPRE_ HT2.0_GPI_2A_dTomato	Duke University Viral Vector Core	GenBank PP719197
AAV10 CAG-CreON_WPRE_ ddHT2.0_GPI_2A_dTomato	Duke University Viral Vector Core	GenBank PP719193
AAV10 CAG-CreON_W3SL_HT2.0_ IRES_dTomato-Farnesylated	VectorBuilder	GenBank PP719195
AAV10 CAG-DIO_mScarlet-HT2.0-GPI (fusion)_WPRE	Duke University Viral Vector Core	N/A
AAV10 CAG-CreON.FlpOFF_W3SL_ HT2.0_IRES_NES-dTomato	VectorBuilder	N/A
AAV10 CAG-CreON.FlpOFF_W3SL_ ddHT2.0_IRES_NES-dTomato	VectorBuilder	N/A
Chemicals, peptides, and recombinant proteins		
NBQX	Tocris Bioscience	Cat #: 1044; CAS: 479347-86-9
CGP54626 hydrochloride	Tocris Bioscience	Cat#: 1088; CAS: 149184-21-4
D-APV	Tocris Bioscience	Cat #: 0106; CAS: 79055-68-8
(RS)-MCPG	Tocris Bioscience	Cat #: 3696; CAS: 146669-29-6
Muscimol	Tocris Bioscience	Cat #: 0289; CAS: 2763-96-4
YM90K.1$^{DART.2}$	Michael Tadross lab, Duke University[29]	Lot # 200725, 221011
Alexa 647.1$^{DART.2}$	Michael Tadross lab, Duke University[29]	Lot # 200213
YM90K.1^{PEG}	Michael Tadross lab, Duke University[29]	Lot # 221011
blank$^{DART.2}$	Michael Tadross lab, Duke University[29]	Lot # 210418
Alexa Fluor^{TM} Carboxylic Acid, tris(triethylammonium) salts	Invitrogen	Cat #: A33084
Deposited data		
Data and code for figures	This paper	figShare: https://doi.org/10.6084/m9.figshare.29174333.v4
Experimental models: Organisms/strains		
CBA	Jackson Labs	000654
SST::Cre	Jackson Labs	013044
PV::Cre	Jackson Labs	008069
Software and algorithms		
ImageJ	NIH	https://micro-manager.org
Micromanager	NIH	https://imagej.nih.gov/ij/
MWorks	MWorks	http://mworks-project.org
pClamp 10 Software Suite	Molecular Devices	N/A
Scanbox	Neurolabware	https://scanbox.org/
MATLAB	Mathworks	https://www.mathworks.com
Python (version 3.8.12)	Python software foundation	https://www.python.org
Code for computational model	This paper	Github: doi.org/10.5281/zenodo.15548282

EXPERIMENTAL MODEL AND SUBJECT DETAILS

Animals. All procedures conformed to standards set forth by the National Institutes of Health Guide for the Care and Use of Laboratory Animals, and were approved by the Duke University's Animal Care and Use Committee. Mice were housed on a normal 12:12 light-dark cycle. Two-photon calcium imaging data in this study were collected from 19 mice (11 female; 14 SST::Cre and 5 PV::Cre). Of these, 12 mice (9 SST::Cre and 3 PV::Cre) were used only in YM90K^{DART} experiments, 5 mice (3 SST::Cre and 2 PV::Cre) were used only in YM90K^{PEG} experiments, and 3 mice (all SST::Cre) were shared. Imaging experiments were conducted at 21–38 weeks of age (mean 27 weeks), except for one mouse imaged at 11 weeks. Headpost, cranial window, and cannula implantation were performed no earlier than 7 weeks, with viral injection a minimum of 3 weeks after. Electrophysiology data were collected from 25 mice (13 female). Electrophysiology experiments were conducted at 5–9 weeks of age. Viral injections for electrophysiology experiments were performed no earlier than 3 weeks of age. All mice for two-photon experiments were either offspring of CBA mice (Jackson Labs, #000654) crossed with SST::Cre (Jackson Labs, #013044) or PV::Cre (Jackson Labs #008069), or offspring of SST::Cre mice crossed with PV::Flp (Jackson Labs, #022730). Mice used for electrophysiology experiments were of these two genotypes, or offspring of SST::Cre mice crossed with R26R-EYFP mice (Jackson Labs, #006148) or crossed with Ai148 mice (Jackson Labs, #030328).

METHOD DETAILS

Surgical procedures

Viruses

Due to the evolving nature of the novel DART reagents,[28,29] we used several constructs for HaloTag protein (HTP) and GCaMP expression over the course of data collection. We have found these to be functionally equivalent. In the methods, viruses are referenced by their identifiers in the following table.

Virus	*Titer (GC/mL)*	*Identifier*
AAV9-pGP-AAV-*syn*-jGCaMP8s-WPRE	4.03x13	GC1
AAV10-pGP-AAV-*syn*-jGCaMP8s-WPRE	6.00x13	GC2
AAV9-pGP-*syn*-jGCaMP8f-WPRE	2.10x13	GC3
AAV10 CAG-CreON_WPRE_HT2.0_GPI_2A_dTomato	2.80x13	HTP1
AAV10 CAG-CreON_WPRE_ddHT2.0_GPI_2A_dTomato	3.50x13	ddHTP1
AAV10 CAG-CreON_W3SL_HT2.0_IRES_dTom-Farnesylated	9.00x12	HTP2
AAV10 CAG-DIO_mScarlet-HT2.0-GPI (fusion)_WPRE	3.07x13	HTP3
AAV10 CAG-CreON.FlpOFF_W3SL_HT2.0_IRES_NES-dTom	2.96x13	HTP4
AAV10 CAG-CreON.FlpOFF_W3SL_ddHT2.0_IRES_NES-dTom	1.86x13	ddHTP2

Intracranial viral injections for electrophysiology

Burrhole injections of viral constructs (HTP1-4, ddHTP1-2) were used to express HTP for slice electrophysiology experiments. Mice were anesthetized with isoflurane (1.2–2% in 100% O2) and positioned in a stereotax (Kopf Instruments). Meloxicam (5 mg/kg) was administered subcutaneously and bupivacaine (5 mg/kg) was administered locally prior to incision. After the skull was exposed, a small hole was drilled +/−2.55 mm lateral from lambda and directly anterior to the lambdoid suture targeting the posterior and medial aspect of the primary visual cortex (V1). For a subset of mice injected under age p28, this coordinate was adjsuted to the individual animal's size by finding the distance between lambda and bregama and dividing by the 4.2mm, then multipling 2.55 by the result. Injection micropipettes were pulled from glass capillary tubes (1B100F-4, World Precision Instruments) and backfilled with virus and then mineral oil and mounted on a Hamilton syringe. The pipette was lowered into the brain and 150–250 nL of virus was pressure injected at 30-50 nL/min using an UltraMicroPump (World Precisions Instruments) 200–250 μm below the surface. We waited 2–3 weeks for viral expression.

Cisterna magna infusion for electrophysiology

For electrophysiology experiments with systemic DART, we introduced YM90K^{DART} (3 mM) and Alexa 647^{DART} (0.3 mM) to the cerebrospinal fluid acutely through injection to the cisterna magna. Meloxicam (5 mg/kg, s.c.) was administered at the start of the surgery. Animals were anesthetized with isoflurane (1.2–2% in 100% O2). An incision was made at the midline at base of the skull and

muscle was displaced by blunt dissection until the membrane of the cisterna magna was accessible. The cisterna magna was located by visual identification. A small puncture was made in the cisterna magna membrane, and 2-5μL of the DART mixture was injected via a 30G needle mounted on a Hamilton syringe. The muscle was replaced and the skin was sutured. Buprenorphine (0.05 mg/kg, s.c.) was delivered upon recovery from anesthesia. Slices for electrophysiology were prepared 2.5–3 h after the cisterna magna injection.

Cranial window implant

Animals were implanted with a titanium headpost and 3–5 mm cranial window. Dexamethasone (3.2 mg/kg, s.c.) was administered at least 2 h before surgery. Animals were anesthetized with ketamine (50 mg/kg, i.p.), xylazine (5 mg/kg, i.p.) and isoflurane (1.2–2% in 100% O2) and given Meloxicam (5 mg/kg, s.c.) as a pre-analgesic. A midline incision was made to expose the skull, and muscle and membranous tissue were scraped away from the exposed bone. A guide cannula (F11552, P1 Technologies) with a complementary dummy cannula (F11372, P1 Technologies) was directed to the right lateral ventricle using the following coordinates from bregma: 1.10 mm lateral, 0.20 mm posterior, 2.30 mm from the skull surface. In a subset of mice, a custom guide cannula was fabricated from 26G stainless steel tubing (taken from Vacutainer Eclipse needles, #368608, BD), with a complementary guide cannula cut from 33G stainless steel wire (GWX-0090-72, Component Supply). The cannula was secured to the skull with C&B Metabond (Parkell). Within the same surgery, a titanium headpost was secured using cyanoacrylate glue and Metabond, and a 3–5 mm craniotomy was made over the left hemisphere (center: 2.8 mm lateral, 0.5 mm anterior to lambda) allowing implantation of a glass window (a 5–8 mm coverslip bonded to two 3–5 mm coverslips (Warner no. 1) with refractive index-matched adhesive (Norland no. 71)) using Metabond. Buprenorphine (0.05 mg/kg) and cefazolin (50 mg/kg) were delivered s.c. every 12 h for 48 h following surgery. Mice were allowed to recover from surgery for a minimum of 7 d before subsequent procedures.

Retinotopic mapping

Following at least 7 d recovery from the headpost implantation surgery, mice were gradually habituated to head restraint. After habituation, mice underwent retinotopic mapping using intrinsic autofluorescence imaging to locate V1 for viral injection. The brain was illuminated with white light (Lumen Dynamics, X-Cite 120) with a 472 ± 30 nm band-pass filter (Edmund Optics), and emitted light was measured through a green and red filter (500 nm longpass). Drifting gratings were presented on a monitor positioned at 45° relative to the body axis, and stimuli were shown at 3 positions (Elevation: −10 deg, Azimuth: −30, 0, and 30 deg, 45° diameter with a Gaussian mask, drifting at 2 Hz, 10 s duration, 10 s inter-trial interval (ITI)) to activate locations in the contralateral visual field. Images were collected using a CCD camera (Rolera EMC-2, QImaging) at 2 Hz through a 5× air immersion objective (0.14 numerical aperture (NA), Mitutoyo), using Micromanager acquisition software (NIH). Images were analyzed in ImageJ (NIH) to measure changes in fluorescence (dF/F; with F being the average of all frames). Injections were targeted to the region of V1 driven by the center stimulus position.

Viral injections for two-photon imaging

The mice used for two-photon imaging underwent an additional surgery for viral injection. Dexamethasone (3.2 mg/kg, s.c.) was administered at least 2 h before surgery. After anesthesia with isoflurane (1.25–2% in 100% O2), the cranial window was removed. HaloTag virus (HTP 2–4) mixed with GCaMP8s (GC 1–2) for SST experiments, or GCaMP8f (GC3) for PV experiments, in a 1:1 ratio was injected via a glass micropipette mounted on a Hamilton syringe. Two hundred to three hundred nanoliters of virus were injected at 170–250 μM below the pia (30-50 nL/min); the pipette was left in the brain for an additional 3 min to allow the virus to infuse into the tissue. Following injection, a new coverslip was sealed in place with Metabond. We then waited a minimum of two weeks for viral expression to mature before performing two-photon experiments.

Experimental procedures

In vitro slice preparation

Mice were deeply anesthetized with isoflurane, the brain was removed and then transferred to oxygenated (95% O_2 and 5% CO_2), ice-cold artificial cerebrospinal fluid (ACSF, in mM: 126 NaCl, 2.5 KCl, 26 $NaHCO_3$, 1.25 NaH_2PO_4, 20 glucose, 2 $CaCl_2$, 1.3 $MgCl_2$). Coronal brain slices (300 μm thickness) were prepared using a vibrating microtome (VT1200S, Leica) and transferred to a holding solution (at 34°C) for 12 min, and then transferred to storage solution for 30 min before being brought to room temperature. The holding solution contained (in mM): 92 NaCl, 2.5 KCl, 1.25 NaH_2PO_4, 30 $NaHCO_3$, 20 HEPES, 25 glucose, 2 thiourea, 5 Na-ascorbate, 3 Na-pyruvate, 2 $CaCl_2$, 2 $MgSO_4$. The storage solution contained (in mM): 93 NMDG, 2.5 KCl, 1.2 NaH_2PO_4, 30 $NaHCO_3$, 20 HEPES, 25 glucose, 2 thiourea, 5 Na-ascorbate, 3 Na-pyruvate, 0.5 $CaCl_2$, 10 $MgSO_4$. For DART incubation (0.5–4 h) we used the same holding solution, with the addition of 1 μM $YM90K^{DART}$ and 0.1 μM $Alexa\ 647^{DART}$. Additional controls used this holding solution with the addition of 1 μM $blank^{DART}$ or 1 μM $YM90K^{PEG}$. Micropipettes pulled from borosilicate glass (1B150F-4, World Precision Instruments) were filled with internal solution containing (in mM): 142 K-gluconate, 3 KCl, 10 HEPES, 0.5 EGTA, 5 phosphocreatine-tris, 5 phosphocreatine-Na2, 3 Mg-ATP, 0.5 GTP. Recording pipettes had resistances of 3–10 MΩ.

In vitro slice recordings

Recordings occurred between 1.5 and 5 h after the animal was sacrificed. Brain slices were transferred to a recording chamber and maintained at 34°C in oxygenated ACSF (containing, in mM: 136 NaCl, 2.5 KCl, 26 $NaHCO_3$, 1.25 NaH_2PO_4, 20 glucose, 2 $CaCl_2$, 1.3 $MgCl_2$, bubbled with 95% O_2 and 5% CO_2) perfused at 2 mL/min. Electrophysiological recordings were restricted to layer 2/3 and V1 was identified by visualization of fluorescence expression at the viral injection site. Neural signals were recorded using a MultiClamp 700B and digitized with a Digidata 1550 (Axon Instruments) with a 20 kHz sample rate. Data acquisition and stimulus presentation was controlled using the Clampex software package (pClamp 10.5, Axon Instruments).

In voltage-clamp recordings, series resistance was monitored using −5 mV steps preceding each trial. Only cells that had <30 MΩ series resistance were included in analysis. Spontaneous EPSCs (sEPSCs; Figures S1A–S1C) were recorded from SST cells, identified by dTomato expression, with cells held at a membrane potential of −85 mV to isolate excitatory events. Following a minimum of 2.5 min in normal ACSF, we washed on NBQX (10 μM, TOCRIS Bioscience) and allowed 2.5 min for NBQX to saturate the slice before collecting data in this condition. To measure evoked EPSC amplitude (Figures 1C, 1D; S1D–S1G), a steel monopolar electrode placed in layer 2/3 near the recorded SST cell, or in between the simultaneously recorded SST and pyramidal cells (~100 μm distance from each cell to electrode). EPSCs were evoked by electrical stimulation (150–250 μA; 100 μs duration); stimulation location and intensity were adjusted prior to data collection to minimize polysynaptic activation (assessed with online observation of EPSCs). Based on our previous data silencing local action potentials with muscimol, we considered monosynaptic responses to be short-latency (<5 ms) EPSCs.[57] All recordings with evoked EPSCs were performed in ACSF containing MCPG (0.4 mM), CGP54626 (1 μM), and APV (30 μM) to block mGluRs, $GABA_B$Rs and NMDARs, respectively. When trains of EPSCs were evoked (50 Hz; Figures S1G–S1I), 50 μM muscimol was included in the ACSF to reduce the contribution of recurrent excitation. For comparison of EPSC amplitudes in $^{+}$HTP SST cells and $^{-}$HTP putative pyramidal cells, we patched nearby pairs (<50 μm distance) and identified SST cells based on dTomato expression and pyramidal cells based on somatodendritic morphology. In a subset of these experiments, DART reagents (300 nM YM90K^{DART} and 100 nM Alexa 647^{DART}) were applied acutely (Figures 1C and 1D and S1G–S1I); in the remainder, DART reagents were infused via the cisterna magna (Figures S1D–S1F). All data are the average of a minimum of 10 trials.

Intracerebroventricular (ICV) infusion

2 μL YM90K^{DART} (3 mM) was co-infused with Alexa 647^{DART} (0.3 mM), while the non-binding YM90K^{PEG} (3 mM) was co-infused with Alexa 647-COOH (0.3 mM). During infusion, mice were headfixed on a running wheel and the dummy cannula removed. An internal cannula (F11373, P1 Technologies) connected to a Hamilton syringe on an infusion pump was inserted into the guide cannula and secured in place. For mice implanted with the custom guide cannula, a custom internal cannula as composed of a 33G hypodermic needle (PRE-33013-100, Steriject) attached to polyethylene tubing (64-0752, Warner Instruments) was used. Compounds were delivered at 75–100 nL/min, followed by at 10–20 min waiting period before the internal cannula was removed. The dummy cannula was then reinserted and secured. For the mice used in both YM90K^{DART} and YM90K^{PEG} experiments, the YM90K^{PEG} infusion and two-photon data collection were always performed at least 48 h prior to the pre-YM90K^{DART} control session.

We visualized Alexa 647^{DART} and Alexa 647-COOH through the cranial window using widefield microscopy. The brain was illuminated with orange light via a 624 ± 40 nm band-pass filter (Edmund Optics) through the cranial window and far-red fluorescence was collected through a 692 ± 40 nm band-pass filter (Edmund Optics). Images were collected using a CCD camera (Rolera EMC-2, QImaging) through a 5× air-immersion objective (0.14 numerical aperture (NA), Mitutoyo) using Micromanager acquisition software (NIH).

Two-photon imaging

Images were collected using a two-photon microscope controlled by Scanbox software (Neurolabware). A Mai Tai eHP DeepSee laser (Newport) was directed into a modulator (Conoptics) and raster scanned on the visual cortex using resonant galvanometers (8 kHz; Cambridge Technology) through a 16X (0.8 NA, Nikon) water-immersion lens at a frame rate of 15 Hz. Emitted photons were directed through a green (510 ± 42 nm band filter; Semrock) or red filter (607 ± 70 nm band filter; Semrock) onto GaAsP photomultipliers (H10770B-40, Hamamatsu). At the start of each experiment, we used an excitation wavelength of 1040 nm to visualize dTomato fluorescence, allowing identification of red SST cells. All functional imaging used an excitation wavelength of 920 nm. Data were collected at 175–250 μM below the cortical surface.

During imaging experiments, mice were head-fixed and allowed to freely run on a cylindrical treadmill. Running speed was monitored with a digital encoder (US Digital). Pupil position was monitored via scattered infrared light from two-photon imaging. Light was collected using a GENIE Nano CMOS camera (Teledyne Dalsa) using a long-pass filter (695 nm) at the imaging rate. For each mouse we performed a baseline imaging session prior to the ICV infusion, and performed a second imaging session 17–24 h later, finding the same plane as in the baseline session using the vasculature and HTP expression as fiduciary markers. For experiments probing epileptiform activity (Figure S7), the second imaging session was performed 4–7 h after infusion.

Visual stimulus presentation

Visual stimuli were presented on a 144-Hz monitor (Asus). The monitor was calibrated with an i1 Display Pro (X-rite) for mean luminance at 60 cd/m2 and positioned 21 cm from the eye. Stimuli were generated and displayed using MWorks (The MWorks Project).

At the beginning of each session, we performed a retinotopy (9 positions, 30 deg diameter gabor grating, 15 deg spacing in azimuth and elevation) to position the monitor such that the receptive fields of the imaged neurons were centered on the screen. During the experiments with SST::Cre mice, full-field, sine-wave gratings (0.1 cycles per degree; 2 Hz) were randomly interleaved at 3 contrasts (25, 50 and 100%) drifting in 8 directions (45 deg increments) for 2 s. During the experiments with PV::Cre mice, sine-wave gratings were randomly interleaved at an additional contrast (12%), size (20 deg with a Gaussian mask) in only 4 directions (0°, 45°, 90° and 135°). Stimuli alternated with a 4 s ITI of uniform mean luminance.

Post-hoc histology

After recording, animals were anesthetized with an overdose of ketamine (200 mg/kg) and xylazine (20 mg/kg) and perfused with PBS followed by 4% PFA in PBS. Brains were dissected and incubated in 4% PFA overnight, rinsed 3x with PBS, then sliced in 70–100 μm sections and mounted on glass slides. Slides were mounted with Fluoromount G with DAPI (Invitrogen) and imaged using an epifluorescence microscope (Keyence BZ-X8100) to confirm overlap of viral expression (GCaMP: excitation- 470 ± 40 nm.,

emission- 525 ± 50 nm; dTomato: excitation- 560 ± 40 nm., emission- 630 ± 75 nm) and capture (Alexa 647: excitation- 605 ± 50 nm., emission- 670 ± 50 nm), and appropriate placement of the cannula in the lateral ventricle.

QUANTIFICATION AND STATISTICAL ANALYSIS

All analyses were performed using custom code written in MATLAB (Mathworks; for electrophysiology and imaging data) or Python (for computational modeling). *N* values refer to number of cells or mice. Sample sizes were not predetermined but were collected to be comparable to published literature for each type of experiment.[39,63–66] Our sample size differs depending on the specific comparison made, as we always used subsets of cells that could be compared across all conditions. The following notation is used throughout the figures, n.s.- not significant; $^{*}p < 0.05$; $^{**}p < 0.01$; $^{***}p < 0.001$.

Electrophysiology

Evoked EPSCs

Amplitudes of EPSCs in response to electrical stimulation were quantified from the mean of the last 10 sweeps of each condition. Amplitudes were calculated as the average response in a 2 ms window around the peak of the response. For measurement of responses to trains of stimuli, the baseline in a window 2 ms before the stimulus artifact was subtracted from the peak to account for the accumulation of current. Cells were excluded from analysis if the resistance changed by more than 20% over the course of the recording. The mean EPSC amplitude for each SST cell was compared to that of the putative pyramidal cell in the same pair to determine the SST:pyramidal EPSC ratio.

Spontaneous EPSCs

Initial event detection was conducted based on rapid changes in the first derivative of the filtered timecourse. Each sweep was passed through a 60Hz bandstop notch filter using the MATLAB *iirnotch* and *filtfilt* functions, and a 4th order 13kHz lowpass Butterworth filter using the MATLAB *butter* and *filtfilt* functions to remove oscillatory noise. The filtered data was then subjected to a median filter over a window of 5 samples using the MATLAB *medfilt1* function, followed by mean smoothing over a window of 1ms using the MATLAB *smooth* function. The first derivative of this filtered data was taken and potential sEPSC onsets were found by identifying points when the slope passed 2 pA/ms. The peak was then identified by finding the first slope reversal after the event onset and finding the maximum value within 2 samples of this slope reversal. The amplitude of each event was calculated as the difference between peak and the mean current in a baseline period spanning 20 ms–5 ms prior to the event. Event offset was determined by finding the first sample at which the trace returned to the baseline value. Events with amplitude smaller than 5 pA, larger than 100 pA, or less than 1ms wide from onset to offset were rejected. These criteria were based on visual inspection of true events compared to noise. Finally, events that overlapped with another ongoing event were rejected.

We included data from ten 10-second sweeps in the ACSF epoch and ten 10-second sweeps in NBQX epoch. The NBQX epoch was set to begin a minimum of 2.5 minutes after arrival of NBQX in the recording chamber, with the start sweep adjusted by manual inspection to begin when event frequency had plateaued. A small number of sweeps (five across two cells) had unclamped action potentials and were removed from analysis. To determine the sEPSC rate, we counted the sEPSCs in each sweep and divided by the sweep length to find events per second, then calculated the average rate across sweeps in each condition. To find the sEPSC amplitude we calculated the mean of the event peak amplitude in each sweep, then calculated the mean across sweeps in each condition. Notably, the threshold of 5 pA causes an underestimate of the change in sEPSC amplitude and an overestimate in the change of frequency.

Two-photon calcium imaging

Registration, segmentation, matching across sessions, and time course extraction

To adjust for x-y motion, we registered all frames from each imaging session to a stable reference image selected out of several 500-frame-average images, using Fourier domain subpixel 2D rigid body registration. For each experiment, we first segmented cells in the YM90K^{DART} session and then used this as a reference to find matching cells in the control session. Cells bodies were manually segmented, first using the dTomato fluorescence to identify HTP+ SST cells, then selecting all other visible cells from images of the average dF/F during stimulus presentation (where F is the average of 1 s preceding each stimulus) for each unique stimulus condition, a time-averaged image of F across the full stack, and a local correlation map (where the value of each pixel is scaled by its correlation with the neighboring 9 pixels). All segmented cells that were not identified based on dTomato fluorescence were labelled as HTP- and assumed to be putative pyramidal cells.

We then found matching cells in the control session. After registration, salient fiduciary marks (e.g. bright cells and thin vasculature) were used to align the image stack to the YM90K^{DART} session. Then, for each cell segmented in the YM90K^{DART} session we examined an approximately 24.5 × 34.5 μM FOV in the corresponding region of the stack from the control session to determine whether the matching cell was detectable. Matching cells were visually identified based on location and morphological similarity to the corresponding cell in the YM90K^{DART} session. Within the small FOV, we used either the dTomato fluorescence (for cells labeled as HTP+ SST in the YM90K^{DART} session), the local correlation map, the time-averaged F across the full stack, or the maximum dF/F projection to identify and manually segment cells in the control session matching those found in the YM90K^{DART} session. Fluorescence time courses were derived by averaging all pixels in a cell mask. To exclude signal from the neuropil, we first selected a three

pixel shell around each neuron (excluding a three pixel boundary around the segmented neuron and the territory of neighboring neurons), then estimated the neuropil scaling factor by maximizing the skew of the resulting subtraction, and finally subtracted this component from each cell's time course.[67]

To ensure that comparisons of dF/F across days or conditions were not impacted by changes to baseline activity or fluorescence, we measured the mean baseline fluorescence (F0) for each cell type across imaging sessions or behavioral states for each experiment. We find no significant differences in F0 following YM90K^{DART}: the ratio of F0 for YM90K^{DART} versus control sessions is 0.999 ± 0.002 (mean ± SEM, stationary trials) for putative pyramidal cells and 1.003 ± 0.003 for SST cells. Likewise, the ratio of F0 in locomotion versus stationary trials is 1.011 ± 0.014 for putative pyramidal cells (control session) and 0.995 ± 0.034 for SST cells. Thus, our comparisons across imaging session and behavioral state reflect changes in visually-evoked neural activity rather than F0.

Visual responses and cell inclusion

Visually-evoked responses were measured as the average dF/F in the 2 s stimulus period starting 3 frames (200 ms) after visual stimulus onset and ending 3 frames after stimulus offset to account for cortical response latency. Among cells that we could identify in both imaging sessions, we included cells that were visually responsive (demonstrated a statistically significant elevation in dF/F during the stimulus period for at least one stimulus condition as defined by a Bonferroni corrected paired t test) in at least one of the sessions. We applied the additional criterion of excluding any cell that had a mean visually evoked response more than 3 standard deviations greater than the mean response of all cells in that imaging session. We then found the preferred direction of visual grating for each cell on each day by identifying the direction with the maximum dF/F response, and all analyses were performed on the subset of trials at that grating direction for each cell.

For analysis of locomotion and arousal, we used subsets of cells that were represented across all conditions. This required that each cell have trials at its preferred direction, for each contrast and state on both imaging sessions. When comparing stationary and locomotion conditions, this stringent inclusion criterion led to the loss of two animals from the YM90K^{DART} experiment and two from the YM90K^{PEG} experiment (these were not the same mice). When comparing small pupil and large pupil conditions, the inclusion criteria excluded a small number of cells, but did not result in the loss of any mice from the sample.

Normalized difference and fraction suppressed or facilitated

As a measure of the impact of YM90K^{DART} on each cell's visual responses, we defined a normalized difference metric:

$$\frac{\text{mean}_{\text{DART}} - \text{mean}_{\text{control}}}{\text{STD}_{\text{control}}}$$

This normalization accounts for the difference in response magnitude across cells. The resulting metric is positive when a cell had a larger response in the YM90K^{DART} session and negative when the cell had a weaker response in the YM90K^{DART} session, compared to the control session. Cells were designated as "suppressed" if the normalized difference was <-1; that is, if the cell's response in the DART session was more than one standard deviation below than that on the control day. Likewise, cells were designated as "facilitated" if the normalized difference was >1. The fraction of cells suppressed or facilitated was calculated by dividing the number of cells that met the above criteria by the total number of cells of that type.

For direct comparison of YM90K^{DART} and YM90K^{PEG} (Figures S2-3) we computed a modulation index for each neuron:

$$\frac{\text{mean}_{\text{YM90K}} - \text{mean}_{\text{control}}}{\text{mean}_{\text{YM90K}} + \text{mean}_{\text{control}}}$$

Cells that had a response <0 during either drug or control sessions were set to 0, so that values are restricted to be between −1 and 1.

SST-Pyr correlation

To separate SST cells into those strongly or weakly correlated with ongoing pyramidal activity, we first found the mean visual response of each SST cell, or the population of neighboring pyramidal cells, to every combination of contrast, direction, and behavioral state. This condition mean was then subtracted from the activity on each trial of that condition and used to calculate the Pearson correlation (using *corrcoef* in MATLAB) for each SST cell with the simultaneously imaged pyramidal population using only stationary trials on the control day. Cells with an R value greater than 0.5 were designated as "strongly correlated" and those with an R value less than 0.5 as "weakly correlated."

Neural Activity Synchrony

For each imaging session, ITI time courses were obtained by concatenating the 30 frames (2s) immediately preceeding each stimulus presentation throughout the neuropil-corrected dF/F time courses. The concatenated ITI time series were then split into 10 equal-length bins, and the mean and standard deviation within each bin was calculated. Cells were deemed active in each frame for having a dF/F value larger than five standard deviations over the mean of that bin, allowing determination of the fraction of active cells on each frame. The synchrony index for each mouse was calculated as the average fraction of cells active over time in the YM90K^{DART} or YM90K^{PEG} divided by that in the control condition.

Neural Activity Entropy

A polygon mask for each session was manually defined based on the viral expression area as appeared on a time-averaged image after registration, using the MATLAB *roipoly* function. A full-session time course was obtained for each polygon mask in the same

manner as the cellular time courses described above. Sample entropy for each full-session time course was calculated using the SampEn (Mathworks File Exchange) function with an embedding dimension of 3 and tolerance at 20%.

Behavioral state determination

Trials were designated as stationary or running based on the mean forward wheel speed during the stimulus period of each trial, with a threshold of 2 cm/s as the threshold for running.

Pupil size and position were extracted from each frame using the native MATLAB function *imfindcircles*, and quantified by averaging all frames during the stimulus period on each trial. To designate large and small pupil trials, we first combined all stationary trials across both imaging sessions, found the median size of this pooled data, and labeled trials with a pupil size less than the median as "small pupil" and those with a pupil size greater than the median as "large pupil."

Capture quantification

To assess capture on HTP+ cells, we analyzed widefield images of Alexa 647 fluorescence collected immediately before the two-photon imaging experiment. In ImageJ, we created a circular ROI around the region of dTomato expression (Figures S1J–S1K), and measured mean fluorescence intensity within this ROI as well as 20-pixel perimeter around the ROI, to assess background fluorescence. We defined the Capture Index as:

$$\left(\frac{\text{mean}_{\text{ROI}}}{\text{mean}_{\text{perimeter}}}\right)$$

where values greater than 1 indicate enrichment of the DART ligands at the site of viral expression.

Computational modeling

Model equations

We started from a four-population rate-based model, including pyramidal (E), PV (P), SST (S) and VIP (V) neuron populations.[4,5,20,21,39] The firing rates of these populations (r_E, r_P, r_S and r_V) obey standard rate equations

$$\begin{cases} \tau_E \frac{dr_E}{dt} = -r_E + \phi_E(W_{EE}r_E - W_{EP}r_P - W_{ES}r_S + I_E) \\ \tau_P \frac{dr_P}{dt} = -r_P + \phi_P(W_{PE}r_E - W_{PP}r_P - W_{PS}r_S + I_P) \\ \tau_S \frac{dr_S}{dt} = -r_S + \phi_S(W_{SE}r_E - W_{SV}r_V + I_S) \\ \tau_V \frac{dr_V}{dt} = -r_V + \phi_V(W_{VE}r_E - W_{VP}r_P - W_{VS}r_S + I_V) \end{cases} \quad \text{(Equation 1)}$$

where W_{AB} is the strength of connections from population B to A, and I_A, τ_A, and ϕ_A are external inputs, time constant and transfer function (F-I curve) of population A. We used rectified-quadratic transfer functions for populations E and S,[33] while for simplicity we used threshold-linear transfer functions for P and V populations:

$$\begin{cases} \phi_{E,S}(x) = a_{E,S}[x]_+^2 \\ \phi_{P,S}(x) = a_{P,V}[x]_+ \end{cases}, \quad \text{(Equation 2)}$$

where $[x]_+ = 0$ for $x < 0$, $[x]_+ = x$ for $x > 0$, while $a_{E,S}$ and $a_{P,V}$ are the gains for quadratic and linear transfer functions.

The influence of YM90K^{DART} is modeled as a decrease in the connection weight from Pyr neurons to SST cells as

$$W_{SE} \rightarrow (1 - x)W_{SE} \quad \text{(Equation 3)}$$

Reduction to a two population (E,S) model

To focus on the interactions between E and S cells, we simplified the four-population model into a two-population circuit composed of pyramidal cells and SST cells (Figures 6A and S5). In a steady state, we can derive from Equation 1, the firing rates of P and V cells as a function of E and S cells exclusively:

$$\begin{cases} r_P = \frac{\phi'_P(W_{PE}r_E - W_{PS}r_S + I_P)}{\phi'_P W_{PP} + 1} \\ r_V = \phi'_V\left[\left(W_{VE} - \frac{W_{VP}W_{PE}}{W_{PP} + 1/\phi'_P}\right)r_E - \left(W_{VS} - \frac{W_{VP}W_{PS}}{W_{PP} + 1/\phi'_P}\right)r_S + I_V - \frac{W_{VP}I_P}{W_{PP} + 1/\phi'_P}\right] \end{cases} \quad \text{(Equation 4)}$$

Combining Equations 1 and 4, the firing rates of pyramidal cells obey

$$\tau_E \frac{dr_E}{dt} = -r_E + \phi_E[(W_{EE} - W_{EPE})r_E - (W_{ES} - W_{EPS})r_S + J_E], \quad \text{(Equation 5)}$$

where $W_{EPE} = \frac{W_{EP}W_{PE}}{1/\phi'_P + W_{PP}}$ is the strength of the feedback of PV interneurons onto pyramidal cells, $W_{EPS} = \frac{W_{EP}W_{PS}}{1/\phi'_P + W_{PP}}$ is the strength of the disinhibition of SST inhibition onto Pyr neurons through PV interneurons, and J_E is an effective external input to Pyr cells, defined as $J_E = I_E - \frac{W_{EP}I_P}{W_{PP}+1/\phi'_P}$ that includes feedforward inhibition from PV cells.

The firing rates of SST cells obey, respectively, in control group and DART group

$$\begin{cases} \tau_S \frac{dr_S}{dt} = -r_S + \phi_S[(W_{SE} - W_{SVE})r_E + W_{SVS}r_S + J_S] \\ \tau_S \frac{dr_S}{dt} = -r_S + \phi_S[((1-x)W_{SE} - W_{SVE})r_E + W_{SVS}r_S + J_S] \end{cases} \quad \text{(Equation 6)}$$

where $W_{SVE} = \phi'_V W_{SV}\left(W_{VE} - \frac{W_{VP}W_{PE}}{W_{PP}+1/\phi'_P}\right)$ describes indirect effects of Pyr cells onto SST cells through VIP cells, $W_{SVS} = \phi'_V W_{SV}\left(W_{VS} - \frac{W_{VP}W_{PS}}{W_{PP}+1/\phi'_P}\right)$ describes the strength of the feedback loop between VIP and SST cells, and J_S is an effective external input to SST cells, defined as $J_S = I_S - \phi'_V W_{SV}\left(I_V - \frac{W_{VP}I_P}{W_{PP}+1/\phi'_P}\right)$ that includes overall inhibition from VIP cells.

Nullclines

The advantage of simplifying the model to two variables is that the dynamics of the model can be visualized on a 2-D plane spanned by the E and S rates. To get insight into the behavior of the model, it is useful to plot nullclines of the system, i.e., the curve on which the E rate is at equilibrium given r_S (the so-called r_E nullcline), and vice versa the curve on which the S rate is at equilibrium given r_E (the r_S nullcline). These nullclines are defined by setting the temporal derivatives of the rates to zero, i.e., $d\frac{r_E}{dt} = 0$ in Equation 5, and $\frac{dr_S}{dt} = 0$ in Equation 6. Fixed points of the network dynamics are then given by the intersections of these two nullclines. We first consider a simplified case where both E and S have linear transfer functions ϕ_E and ϕ_S. In this case, the nullclines are given by:

$$\begin{cases} r_E = (\tilde{W}_{EE} - \tilde{W}_{EPE})r_E - (\tilde{W}_{ES} - \tilde{W}_{EPS})r_S + J_E \\ r_{S(control)} = (\tilde{W}_{SE} - \tilde{W}_{SVE})r_E + \tilde{W}_{SVS}r_S + J_S \\ r_{S(DART)} = ((1-x)\tilde{W}_{SE} - \tilde{W}_{SVE})r_E + \tilde{W}_{SVS}r_S + J_S \end{cases} \quad \text{(Equation 7)}$$

where $\tilde{W}_{AB} = \phi'_A W_{AB}$ for all A,B = E,S, and $\tilde{W}_{ACB} = \phi'_A W_{AB}$ for all A,B = E,S and C=P,V. From Equation 7, we find that the r_S nullcline increases monotonically with r_E, with a slope that decreases in the DART condition, provided $\tilde{W}_{SE} > \tilde{W}_{SVE}$ *and* $\tilde{W}_{SVS} < 1$

$$\begin{cases} r_{S(control)} = \frac{(\tilde{W}_{SE} - \tilde{W}_{SVE})r_E + J_S}{1 - \tilde{W}_{SVS}} \\ r_{S(DART)} = \frac{((1-x)\tilde{W}_{SE} - \tilde{W}_{SVE})r_E + J_S}{1 - \tilde{W}_{SVS}} \end{cases} \quad \text{(Equation 8)}$$

The r_E nullcline is given by:

$$r_E = \frac{(\tilde{W}_{EE} - \tilde{W}_{EPE} - 1)r_E + J_E}{\tilde{W}_{ES} - \tilde{W}_{EPS}} \quad \text{(Equation 9)}$$

The sign of the slope of the r_E nullcline is determined by the sign of $\tilde{W}_{EE} - \tilde{W}_{EPE} - 1$ and $\tilde{W}_{ES}$-$\tilde{W}_{EPS}$. When $\tilde{W}_{EE} < \tilde{W}_{EPE} + 1$ and $\tilde{W}_{ES} > \tilde{W}_{EPS}$, the slope of the r_E nullcline is negative (region R_i). Thus, in this region, YM90K^{DART} leads to an increase in r_E and a decrease in r_S. When $\tilde{W}_{EE} > \tilde{W}_{EPE} + 1$ and $\tilde{W}_{ES} > \tilde{W}^{\star}_{EPS}$, the slope of r_E nullcline becomes positive (region R_{ii}). Thus, in this region, YM90K^{DART} leads to an increase of both r_E and r_S. When $\tilde{W}_{EE} < \tilde{W}_{EPE} + 1$ and $\tilde{W}_{ES} < \tilde{W}_{EPS}$, the slope of r_E nullcline is again positive (region R_{iii}), but YM90K^{DART} leads to a decrease of both r_E and r_S (Figures 6B–6D). The characteristics of each region can be summarized as follows:

Region	slope of r_E nullcline	Numerator	Denominator	YM90K^{DART} effect
R_i	(−)	(−): $\tilde{W}_{EE} < \tilde{W}_{EPE} + 1$	(+): $\tilde{W}_{ES} > \tilde{W}_{EPS}$	↓S ↑E
R_{ii}	(+)	(+): $\tilde{W}_{EE} > \tilde{W}_{EPE} + 1$	(+): $\tilde{W}_{ES} > \tilde{W}_{EPS}$	↑S ↑E
R_{iii}	(+)	(−): $\tilde{W}_{EE} < \tilde{W}_{EPE} + 1$	(−): $\tilde{W}_{ES} < \tilde{W}_{EPS}$	↓S ↓E

Instability line

The stability of the fixed points of Equations 5 and 6 can be determined by computing the eigenvalues of the Jacobian matrix of the system. In particular, a "rate" instability is reached whenever the Jacobian matrix has a zero eigenvalue, or equivalently $Det(J) = 0$ where J is the Jacobian matrix. This condition leads to

$$(\tilde{W}_{EE} - \tilde{W}_{EPE} - 1)(\tilde{W}_{SVS} - 1) - (\tilde{W}_{EPS} - \tilde{W}_{ES})[(\tilde{W}_{SE} - \tilde{W}_{SVE})] = 0, \quad \text{(Equation 10)}$$

or equivalently

$$\tilde{W}_{ES} - \tilde{W}_{EPS} = \frac{1 - \tilde{W}_{SVS}}{(\tilde{W}_{SE} - \tilde{W}_{SVE})}(\tilde{W}_{EE} - \tilde{W}_{EPE} - 1) \quad \text{(Equation 11)}$$

This line is plotted in Figures 6 and 7. Equations 5 and 6 also potentially exhibit oscillatory instabilities in the ISN region, that depend on time constants in addition to effective weights. We checked that for parameters fitting the data, the model is stable with respect to such oscillatory instabilities. However, the model tends to develop damped oscillations in response to high contrast inputs, consistent with experimental observations in mouse visual cortex.[55]

Fitting procedure

The equations of the reduced two population model show that the fixed point of network equations depend only on five parameters involving the couplings: $W_{EE} - W_{EPE}, W_{ES} - W_{EPS}, W_{SE}, W_{SVP}, W_{SVS}$. These equations also depend on x, the fractional reduction of AMPA receptor conductance by YM90K^{DART}, and external inputs J_E, J_S. We used three variants of the model (Full, VIP, and Input; Figure 7D; S6A and S6B), that differ according to which parameters depend on state. In all models, external inputs depend on both contrast and state, and coupling strengths are independent of contrast. For both states and all contrasts, external inputs were constrained to produce the experimentally observed rates in control condition,

$$\begin{cases} J_E = \phi_E^{-1}(r_E) - (W_{EE} - W_{EPE})r_E + (W_{ES} - W_{EPS})r_S \\ J_S = \phi_S^{-1}(r_S) - (W_{SE} - W_{SVE})r_E - W_{SVS}r_S \end{cases} \quad \text{(Equation 12)}$$

where the parameters $a_{E,S}$ and $a_{P,V}$ were chosen such that the slopes of the transfer function are equal to one in the 50% contrast, running condition. In the Full model, all coupling strengths depend on state. In the VIP model, all synaptic strengths are independent of state, but the gain of the VIP population ϕ'_V depends on state. We denote by g the ratio between VIP gain in running and stationary conditions. Note that this change only affects the effective weights that depends on VIP gain, i.e., W_{SVE} and W_{SVS}. Finally, in the Input model, all weight parameters are fixed and independent of state. In all variants, x is a fixed parameter, independent of contrast and state. The value of x was set to 0.5, but we found that the minimum of the cost function C is independent of x, provided effective weights onto SST cells are varied accordingly (see below).

We defined a cost function C as

$$C = \Sigma_{p,c,\sigma}\left(r_{p,c,\sigma}(\text{model}) - r_{p,c,\sigma}(\text{data})\right)^2 \Big/ SE_{p,c,\sigma}(\text{data})^2, \quad \text{(Equation 13)}$$

where the sum over p is a sum over populations ($p = E, S$), $c = 25\%, 50\%, 100\%$ is the contrast, and $\sigma =$ stationary, running is the state. Note that in Equation 10 only the YM90K^{DART} condition enters, since by construction all models in all conditions match the data perfectly in control conditions, provided the system converges to a fixed point. In some cases, the fixed point becomes unstable and the system converges to an oscillatory state, leading to a small discrepancy between model and data in control conditions. This happens in particular for the best fit 'Input' model at high contrast in running conditions (Figure S6B).

For each parameter set, modeled rates were obtained by simulating model equations. We then used the *differential_evolution* optimization algorithms from Python package *SciPy.optimize* to obtain the minimum of the cost function. We constrained the absolute value of all weight parameters to be smaller than 10, to avoid convergence to unrealistically large values of such parameters. For model selection, we used the Akaike Information Criterion (AIC).[47] The optimal parameters found by this approach are shown in Table S4 for the VIP model, and Tables S3 and S5 for the Full and Input models.

To show that the minimum of the cost function is independent of x, we first note that in control and YM90K^{DART} groups, Pyr influences SST through effective weights A (in control) and B (in YM90K^{DART}),

$$\begin{cases} A = W_{SE} - W_{SVE} \\ B = (1 - x)W_{SE} - W_{SVE} \end{cases} \quad \text{(Equation 14)}$$

Once W_{SE} and W_{SVE} are found for a particular value of x, their values for arbitrary values of x can be obtained using

$$\begin{cases} W_{SE} = (A - B)/x \\ W_{SVE} = (A - B)/x - A \end{cases} \quad \text{(Equation 15)}$$

As x increases, W_{SE} and W_{SVE} decrease monotonically (Figure S6C). While W_{SE} is always positive (as it should be), W_{SVE} becomes negative for large enough x, which means that the indirect effect of Pyr → PV→ VIP→ SST disinhibitory pathway is stronger than the Pyr→ VIP→ SST inhibitory pathway.

Simulated optogenetic suppression

To simulate optogenetic suppression of SST cells, we added a negative hyperpolarizing input $J_{S,opto}$ to J_S in Equation 6. For these simulations, we modified the transfer functions so that they become linear at high rates, to avoid pathological effects due to unrealistically high slopes of these transfer functions for high input currents. For both E and S populations, we defined a current at which the transfer function switches from quadratic to linear, which we took to be the stationary current in the condition for which the firing rates of both populations are highest. The parameters of the linear part were then chosen so that both transfer function and its derivative are continuous at this transition current. In Figure S7 we show the resulting dynamics for $J_{S,opto} = -1$ (weak suppression) and $J_{S,opto} = -10$ (strong suppression). To simulate optogenetic suppression of PV cells, we added a negative hyperpolarizing input $I_{P,opto}$ to I_P, and then used the relationship between J_E and J_S and I_P, $J_E = I_E - k_{EP}I_P$ and $J_S = I_S - \phi'_V W_{SV} I_V + k_{SP} I_P$, where $k_{EP} = \frac{W_{EP}}{W_{PP}+1/\phi'_P}$ and $k_{SP} = \phi'_V W_{SV} \frac{W_{VP}}{W_{PP}+1/\phi'_P}$. As our fits do not fully constrain k_{EP} and k_{SP}, we used previous studies that have fitted such parameters from other experimental data[5,10] to set $k_{EP} = 2$ and $k_{SP} = 1$. In Figure S7 we show the resulting dynamics for $I_{P,opto} = -1$.